

Article

Tuning Cu-Content $\text{La}_{1-x}\text{Sr}_x\text{Ni}_{1-y}\text{Cu}_y\text{O}_{3-\delta}$ with Strontium Doping as Cobalt-Free Cathode Materials for High-Performance Anode-Supported IT-SOFCs

Jakub Lach ¹, Kun Zheng ^{1,2,*}, Ryszard Kluczowski ^{3,4}, Anna Niemczyk ^{4,5}, Hailei Zhao ^{6,7} and Min Chen ⁸

¹ Department of Hydrogen Energy, Faculty of Energy and Fuels, AGH University of Science and Technology, al. A. Mickiewicza 30, 30-059 Krakow, Poland

² AGH Centre of Energy, AGH University of Science and Technology, ul. Czarnowiejska 36, 30-054 Krakow, Poland

³ Ceramic Department CEREL, Institute of Power Engineering, Techniczna 1, 36-040 Boguchwala, Poland

⁴ Institute of Power Engineering, Mory 8, 01-330 Warsaw, Poland

⁵ Center for Hydrogen Technologies (CTH2), Institute of Power Engineering, Augustowka 36, 02-981 Warsaw, Poland

⁶ School of Materials Science and Engineering, University of Science and Technology Beijing, Beijing 100083, China

⁷ Beijing Key Lab. of New Energy Materials and Technology, Beijing 100083, China

⁸ School of Materials Science and Energy Engineering, Foshan University, Foshan 528000, China

* Correspondence: zheng@agh.edu.pl



Citation: Lach, J.; Zheng, K.; Kluczowski, R.; Niemczyk, A.; Zhao, H.; Chen, M. Tuning Cu-Content $\text{La}_{1-x}\text{Sr}_x\text{Ni}_{1-y}\text{Cu}_y\text{O}_{3-\delta}$ with Strontium Doping as Cobalt-Free Cathode Materials for High-Performance Anode-Supported IT-SOFCs. *Materials* **2022**, *15*, 8737. <https://doi.org/10.3390/ma15248737>

Academic Editor: Giovanni Battista Appetecchi

Received: 8 November 2022

Accepted: 6 December 2022

Published: 7 December 2022

Publisher's Note: MDPI stays neutral with regard to jurisdictional claims in published maps and institutional affiliations.



Copyright: © 2022 by the authors. Licensee MDPI, Basel, Switzerland. This article is an open access article distributed under the terms and conditions of the Creative Commons Attribution (CC BY) license (<https://creativecommons.org/licenses/by/4.0/>).

Abstract: Cu-content $\text{La}_{1-x}\text{Sr}_x\text{Ni}_{1-y}\text{Cu}_y\text{O}_{3-\delta}$ perovskites with A-site strontium doping have been tuned as cobalt-free cathode materials for high-performance anode-supported SOFCs, working at an intermediate-temperature range. All obtained oxides belong to the $R\text{-}3c$ trigonal system, and phase transitions from the $R\text{-}3c$ space group to a $Pm\text{-}3m$ simple perovskite have been observed by HT-XRD studies. The substitution of lanthanum with strontium lowers the phase transition temperature, while increasing the thermal expansion coefficient (TEC) and oxygen non-stoichiometry δ of the studied materials. The thermal expansion is anisotropic, and TEC values are similar to commonly used solid electrolytes (e.g., $14.1 \times 10^{-6} \text{ K}^{-1}$ for $\text{La}_{0.95}\text{Sr}_{0.05}\text{Ni}_{0.5}\text{Cu}_{0.5}\text{O}_{3-\delta}$). The oxygen content of investigated compounds has been determined as a function of temperature. All studied materials are chemically compatible with GDC-10 but react with LSGM and 8YSZ electrolytes. The anode-supported SOFC with a $\text{La}_{0.95}\text{Sr}_{0.05}\text{Ni}_{0.5}\text{Cu}_{0.5}\text{O}_{3-\delta}$ cathode presents an excellent power density of $445 \text{ mW}\cdot\text{cm}^{-2}$ at $650 \text{ }^\circ\text{C}$ in humidified H_2 . The results indicate that $\text{La}_{1-x}\text{Sr}_x\text{Ni}_{1-y}\text{Cu}_y\text{O}_{3-\delta}$ perovskites with strontium doping at the A-site can be qualified as promising cathode candidates for anode-supported SOFCs, yielding promising electrochemical performance in the intermediate-temperature range.

Keywords: cathode materials; Cu-rich perovskites; Sr doping in $(\text{LaSr})(\text{NiCu})\text{O}_3$; intermediate-temperature solid oxide fuel cells; anode-supported SOFCs

1. Introduction

Various types of energy storage and conversion technology are under development to balance the mismatch of supply and demand for energy sources, including wind and solar renewables, which are considered to be a form of intermittent power and connected with numerous aspects, such as weather variations and geographic location. The solid oxide fuel cell (SOFC) is one of the most favorable energy conversion and storage devices, which can be scaled up for decentralized energy applications [1–4]. SOFCs possess the capability to produce electricity and heat using the fuel and to store surplus electricity when demand is low in the fuel within electrolysis mode (the reversed operation of SOFC). Good power yields (exceeding $1000 \text{ mW}\cdot\text{cm}^{-2}$) of SOFCs are usually observed at a rather high temperature range (above $800 \text{ }^\circ\text{C}$) [5]. The high working temperature of SOFCs leads

to considerably high operational costs, and it also limits the choice of device materials, making SOFCs still unmarketable. Therefore, the commercial application of SOFCs requires a lowering of the operation temperature to an intermediate range (500–750 °C), while still maintaining high cell power density [6,7]. To bring down the working temperature of SOFCs, electrodes with highly electrocatalytic activity and stability are required to enable a reasonable power output. For intermediate-temperature solid oxide fuel cells (IT-SOFCs), the electrochemical performance deterioration of the cathode at reduced temperatures has a huge impact on output power. An effectively working cathode with excellent efficiency in oxygen reduction and evolution reactions at an intermediate-temperature range is a requisite to providing the stable and high performance of IT-SOFCs [7–9].

The perovskite ($ABO_{3-\delta}$) or perovskite-related structured oxide is one group of the most interesting and comprehensively studied cathode material candidates for IT-SOFCs, presenting great potential in chemical composition modifications, yielding the design and gain of desired physicochemical (including mixed ionic–electronic transport properties) and electrochemical properties [7,10]. Cobalt-based perovskites, including $La_{1-x}Sr_xCo_{1-y}Fe_yO_{3-\delta}$ [11–13] and $Ba_{1-x}Sr_xCo_{1-y}Fe_yO_{3-\delta}$ compounds [9,13], were systematically investigated as cathode materials for IT-SOFCs, presenting promising mixed ionic–electronic conductivity and excellent electrocatalytic reactivity for oxygen reduction reactions [14,15]. In addition, double perovskites with a formula of $Ln_{2-x}(Ba,Sr)_xCo_{2-y}M_yO_{5+\delta}$ (Ln: lanthanides M: 3d metals) [16–19] present very fast oxygen ionic transport, related to the layered structure, contributing to a favorable performance in IT-SOFCs. However, the shortcomings of cobalt-containing compounds related to the very high thermal expansion coefficient [20–22], negative environmental impact, and high price of cobalt [23,24] significantly limit their commercial applications. Therefore, the development of cobalt-free alternatives with high performance is of importance [25,26]. Cu-content materials featuring favorable physicochemical properties belong to the group of promising alternative cathode materials for SOFCs [25]. For example, $La_4BaCu_5O_{13\pm\delta}$, featuring a low cathodic polarization value of $0.03 \Omega \cdot cm^2$ at 900 °C, was proposed as a novel cathode for SOFCs, enabling the achievement of a favorable power yield exceeding $1000 mW \cdot cm^{-2}$ at 900 °C [27]. The triple perovskite $La_{1.5}Ba_{1.5}Cu_3O_{7\pm\delta}$ was investigated as a Co-free cathode candidate for SOFCs, exhibiting a very low polarization value of $0.019 \Omega \cdot cm^2$ and a relatively high performance of $458 mW \cdot cm^{-2}$ at 750 °C [28]. The $Ln(Ba,Sr)Cu_2O_{5+\delta}$ (Ln: Nd and Sm)-layered double perovskites were also studied as cathode candidates for IT-SOFCs, presenting relatively low thermal expansion coefficients and good electrochemical properties [29–31]. $Ln_2CuO_{4+\delta}$ -type (Ln: lanthanides) Ruddlesden–Popper oxides with the presence of interstitial oxygen favoring ionic transport were systematically explored as new cathodes for SOFCs [32–35].

The simple perovskite $LaCuO_3$ is one of the well-studied Cu-content oxides with a superior high conductivity ($10^6 S \cdot cm^{-1}$) [36]. However, the stoichiometric $LaCuO_3$ perovskite can be hardly obtained and suffers with stability issues in air [37,38]. The cation-doping strategy should be applied to stabilize the perovskite structure. It has been noted that the $LaCo_{0.4}Ni_{0.4}Cu_{0.2}O_{3-\delta}$ simple perovskite possesses very high electrical conductivity ($1480 S \cdot cm^{-1}$ at 500 °C), yielding a good peak power output at 700 °C ($535 mW \cdot cm^{-2}$) [39]. For Cu- and Ni-containing $LaNi_{0.5}Cu_{0.5}O_{3-\delta}$ compounds, a desirable low cathodic polarization of $0.056 \Omega \cdot cm^2$ was achieved at 800 °C, and a relatively high power output of $870 mW \cdot cm^{-2}$ was recorded at 900 °C [40]. The generation of oxygen vacancies can be particularly advantageous for cathode materials, favoring an increase in the ionic conductivity component [41]. The beneficial effect of strontium doping in the $La_{2-x}Sr_xNiO_{4+\delta}$ system was reported to enhance the structure stability of La_2NiO_4 by increasing the bond length of $La(Sr)-O$ [42]. The substitution of La with Sr in $La_{2-x}Sr_xNiO_{4+\delta}$ materials is favorable, contributing to the reduction in cathodic polarization and the increase in SOFC power density [43]. The valuable outcome of the Sr dopant was also confirmed by the reduction in oxygen vacancy formation energy in perovskite oxides $La_{1-x}Sr_xMO_{3-\delta}$ (M = Fe, Mn) [44]. Therefore, in this work, Cu-content $La_{1-x}Sr_xNi_{1-y}Cu_yO_{3-\delta}$ oxides with strontium doping at the A-site were evaluated as very promising cobalt-free cathode material candidates for

IT-SOFCs. The introduction of strontium at the A-site should result in an increase in oxygen non-stoichiometry δ in the proposed compounds. Physicochemical properties regarding crystal structure, phase transition, thermal expansion properties, oxygen content change as a function of temperature, chemical stability, and the compatibility of studied materials with commonly used solid electrolytes, as well as the electrochemical performance, were systematically investigated.

2. Materials and Methods

Soft chemistry methods were applied to synthesize the $\text{La}_{1-x}\text{Sr}_x\text{Ni}_{1-y}\text{Cu}_y\text{O}_{3-\delta}$ oxides. Stoichiometric amounts of La_2O_3 , SrCO_3 , $\text{Ni}(\text{NO}_3)_2 \cdot 6\text{H}_2\text{O}$, and $\text{Cu}(\text{NO}_3)_2 \cdot 6\text{H}_2\text{O}$ (all with purity $\geq 99.9\%$) were respectively dissolved in a HNO_3 solution. Then, citric acid and ethylenediaminetetraacetic acid (as the complexing agent) were added during stirring at a molar ratio of 1:1 and 1.5:1, respectively, in relation to the total amount of all cations, and ammonia was added to neutralize the solutions to a pH value of 7. The obtained homogeneous solutions were slowly heated in quartz containers to around 400°C . During the heating process, water evaporation, the decomposition of excessive ammonia nitrates and the oxidation of residual carbon occurred. The obtained precursors were well grounded and fired in air at 800°C for 12 h. The $\text{La}_{1-x}\text{Sr}_x\text{Ni}_{0.75}\text{Cu}_{0.25}\text{O}_{3-\delta}$ ($x = 0$ and 0.05) and $\text{LaNi}_{0.5}\text{Cu}_{0.5}\text{O}_{3-\delta}$ compounds were successfully synthesized in air at 800°C for 12 h. For the $\text{La}_{0.9}\text{Sr}_{0.1}\text{Ni}_{0.75}\text{Cu}_{0.25}\text{O}_{3-\delta}$ and $\text{La}_{0.95}\text{Sr}_{0.05}\text{Ni}_{0.5}\text{Cu}_{0.5}\text{O}_{3-\delta}$ oxides, additional heating, regrinding, and sintering at 800°C for 12 h in pure oxygen were conducted to obtain single-phase materials. However, the synthesis of materials with a further increase in strontium doping did not succeed, despite trying additional heating, regrinding, and sintering at different temperatures (800 – 1000°C) and atmospheres (air, oxygen and argon).

The crystal structure at room temperature (RT) of the obtained compounds was investigated by XRD studies using a Panalytical Empyrean diffractometer in the 10 – 110 deg range with $\text{CuK}\alpha$ radiation. High-temperature XRD (HT-XRD) studies were performed on a Panalytical Empyrean apparatus equipped with an Anton Paar HTK 1200N (Graz, Austria) oven chamber. The refinement of the collected XRD data was performed using the Rietveld method with a GSAS/EXPGUI-II set of software [45,46]. Particle size analysis of the powders of $\text{La}_{1-x}\text{Sr}_x\text{Ni}_{0.75}\text{Cu}_{0.25}\text{O}_{3-\delta}$ ($x = 0, 0.05$ and 0.1) and $\text{La}_{1-x}\text{Sr}_x\text{Ni}_{0.5}\text{Cu}_{0.5}\text{O}_{3-\delta}$ ($x = 0$ and 0.05) was performed using the Mastersizer 3000 laser-diffraction particle-size analyzer (Malvern Panalytical, Malvern, UK). Scanning electron microscopy (SEM) measurements were performed using ThermoFisher Scientific Phenom XL Desktop SEM apparatus on the powders obtained (Waltham, MA, USA). Thermal expansion studies of sinters in air up to 800°C were carried out on a Linseis L75 Platinum Series dilatometer (Selb, Germany). Titration measurements were performed to determine the oxygen content in the studied materials using the EM40-BNC Mettler Toledo titrator with a platinum electrode (Mettler-Toledo, Poland). The oxygen content of the investigated compounds was calculated using the average values from three titration measurements. Thermogravimetric (TG) measurements were performed on TA Instruments Q5000IR (New Castle, DE, USA) apparatus from RT to 800°C , with a heating rate of 2°min^{-1} , and the buoyancy effect was taken into account. The chemical stability and compatibility studies of the $\text{La}_{1-x}\text{Sr}_x\text{Ni}_{0.75}\text{Cu}_{0.25}\text{O}_{3-\delta}$ ($x = 0, 0.05$ and 0.1) and $\text{La}_{1-x}\text{Sr}_x\text{Ni}_{0.5}\text{Cu}_{0.5}\text{O}_{3-\delta}$ ($x = 0$ and 0.05) oxides towards typical solid electrolytes CGO10 ($\text{Ce}_{0.9}\text{Gd}_{0.1}\text{O}_{1.95}$), LSGM ($\text{La}_{0.8}\text{Sr}_{0.2}\text{Ga}_{0.8}\text{Mg}_{0.2}\text{O}_{3-d}$), and 8YSZ (8 mol% yttria stabilized zirconia) were studied by analyzing the collected XRD data for the respective compound and solid electrolyte mixtures (with a ratio of 50:50 wt.%), which were fired in air at 800°C for 100 h.

As the anode-supported SOFC design considerably decreases the cell's ohmic resistance and maximizes the power output [47], in this work, anode-supported IT-SOFCs were fabricated with the considered cathode material. The anode-supported half-cells with Ni-8YSZ | 8YSZ | CGO10 configuration were provided by the Ceramic Department CEREL, Institute of Power Engineering, Poland. The anode functional layer (around $7\ \mu\text{m}$) was deposited on the anode substrate of $1000\ \mu\text{m}$, and the 8YSZ electrolyte ($\sim 6\ \mu\text{m}$) with a

CGO10 buffer (~6 μm) was applied. The details of the standard fabrication procedures of the anode-supported half-cells at the Institute of Power Engineering can be found in [48,49]. Cathode paste was prepared by the well mixing of grinded cathode material powder with an appropriate amount of a texanol-based binder, and the cathode layer (with a thickness of ~30 μm) was fired at 800 $^{\circ}\text{C}$ for 2 h in air. The area of the cathode in the constructed cells was approx. 0.25 cm^2 . Pt wires and Ag mesh were used as current collectors in tested cells. Cells were fueled by wet (ca. 3 vol% H_2O) H_2 with a gas flow of 40 $\text{cm}^3 \text{min}^{-1}$ and air flow for the cathode. SOFC performance was characterized using the Solartron SI 1287 interface and Solartron 1252A analyzer. Impedance spectroscopy studies were conducted under open-circuit conditions with a 25 mV amplitude in a 0.1–300 kHz range. The electrochemical impedance spectroscopy data were fitted with a $L\text{-}R_{\text{ohm}}\text{-(RQ)}_{\text{HF}}\text{-(RQ)}_{\text{LF}}$ equivalent circuit, where L represents the inductance, R_{ohm} —ohmic represents the resistance, and RQ is the resistance and constant phase elements, which can be related to processes occurring at high frequencies (HFs) and low frequencies (LFs) [50].

3. Results and Discussion

3.1. Crystal Structure Properties and Microstructure

As reported in our previous work [40], high Cu-content $\text{LaNi}_{1-y}\text{Cu}_y\text{O}_{3-\delta}$ perovskites present attractive physicochemical and electrochemical properties as air electrode materials for SOFCs, especially $\text{LaNi}_{0.5}\text{Cu}_{0.5}\text{O}_{3-\delta}$ cathode material. The substitution of La with Sr at the A-site of $\text{La}_{1-x}\text{Sr}_x\text{Ni}_{1-y}\text{Cu}_y\text{O}_{3-\delta}$ perovskites contributes to an increase in oxygen vacancies in the compounds, thus enhancing ionic conductivity. As shown in Figure 1, the above-described soft chemistry synthesis method yielded $\text{La}_{1-x}\text{Sr}_x\text{Ni}_{0.75}\text{Cu}_{0.25}\text{O}_{3-\delta}$ ($x = 0$ and 0.05) single-phase compounds without the presence of any impurities. Meanwhile, for the $\text{La}_{0.9}\text{Sr}_{0.1}\text{Ni}_{0.75}\text{Cu}_{0.25}\text{O}_{3-\delta}$ oxide, very minor CuO and NiO secondary phases were observed, and a further introduction of strontium at the A-site led to the presence of a large number of impurities (see Figure 1d). Therefore, the maximum doping level of strontium in $\text{La}_{1-x}\text{Sr}_x\text{Ni}_{0.75}\text{Cu}_{0.25}\text{O}_{3-\delta}$ is limited to $x = 0.1$. The crystal structure of $\text{La}_{1-x}\text{Sr}_x\text{Ni}_{0.75}\text{Cu}_{0.25}\text{O}_{3-\delta}$ ($x = 0, 0.05$ and 0.1) can be refined using a rhombohedral structure with the $R\text{-}3c$ space group, typical for the LaNiO_3 [51], LaCuO_3 [37], and Cu-containing $\text{LaNi}_{0.75}\text{Cu}_{0.25}\text{O}_{3-\delta}$ [40] perovskites. Rietveld refinement results for $\text{La}_{1-x}\text{Sr}_x\text{Ni}_{0.75}\text{Cu}_{0.25}\text{O}_{3-\delta}$ ($x = 0, 0.05$ and 0.1), including unit cell parameters and volume, are gathered in Table 1. As can be derived from the results, the increase in Sr content at the La-site causes a decrease in the unit cell volume of $\text{La}_{1-x}\text{Sr}_x\text{Ni}_{0.75}\text{Cu}_{0.25}\text{O}_{3-\delta}$ ($x = 0, 0.05$ and 0.1) (Table 1). This is related to the fact that an increase in Sr content causes an increase in the concentration of oxygen vacancies [52] and the average oxidation states of B-site cations, which were confirmed by the following TG measurements and titration analysis. In addition, B-site cations with high oxidation states strengthen the B-O bond in the BO_6 structure block, thus decreasing the unit cell volume of the perovskite. The observed decrease in density with the increase in Sr doping for $\text{La}_{1-x}\text{Sr}_x\text{Ni}_{0.75}\text{Cu}_{0.25}\text{O}_{3-\delta}$ ($x = 0, 0.05$ and 0.1) oxides was due to the substitution of heavy lanthanum with light strontium.

Table 1. Rietveld refinement results for as-synthesized $\text{La}_{1-x}\text{Sr}_x\text{Ni}_{1-y}\text{Cu}_y\text{O}_{3-\delta}$ oxides.

| Composition | Space Group | a = b [Å] | c [Å] | V [Å ³] | Density [g/cm ³] | R _p [%] | R _{wp} [%] |
|---|---------------|-----------|------------|---------------------|------------------------------|--------------------|---------------------|
| $\text{LaNi}_{0.75}\text{Cu}_{0.25}\text{O}_{3-\delta}$ | $R\text{-}3c$ | 5.4687(1) | 13.1877(1) | 341.56(1) | 7.20 | 4.22 | 6.64 |
| $\text{La}_{0.95}\text{Sr}_{0.05}\text{Ni}_{0.75}\text{Cu}_{0.25}\text{O}_{3-\delta}$ | $R\text{-}3c$ | 5.4591(1) | 13.1814(1) | 340.21(1) | 7.15 | 3.64 | 2.51 |
| $\text{La}_{0.9}\text{Sr}_{0.1}\text{Ni}_{0.75}\text{Cu}_{0.25}\text{O}_{3-\delta}$ | $R\text{-}3c$ | 5.4539(1) | 13.2055(1) | 340.17(1) | 7.08 | 4.80 | 3.21 |
| $\text{LaNi}_{0.5}\text{Cu}_{0.5}\text{O}_{3-\delta}$ | $R\text{-}3c$ | 5.4730(1) | 13.2166(1) | 342.85(1) | 7.19 | 4.19 | 2.97 |
| $\text{La}_{0.95}\text{Sr}_{0.05}\text{Ni}_{0.5}\text{Cu}_{0.5}\text{O}_{3-\delta}$ | $R\text{-}3c$ | 5.4660(1) | 13.2318(1) | 342.37(1) | 7.14 | 4.24 | 3.00 |

XRD data, together with Rietveld refinement for the $\text{La}_{1-x}\text{Sr}_x\text{Ni}_{0.5}\text{Cu}_{0.5}\text{O}_{3-\delta}$ ($x = 0$ and 0.05) oxides, are presented in Figure 2, and the refined data are shown in Table 1. However, further strontium doping in $\text{La}_{1-x}\text{Sr}_x\text{Ni}_{0.5}\text{Cu}_{0.5}\text{O}_{3-\delta}$ did not succeed. Sr doping did not change the crystal structure of the studied materials. $\text{LaNi}_{0.5}\text{Cu}_{0.5}\text{O}_{3-\delta}$ and $\text{La}_{0.95}\text{Sr}_{0.05}\text{Ni}_{0.5}\text{Cu}_{0.5}\text{O}_{3-\delta}$ compounds possess the same crystal structure as the $R\bar{3}c$ space group. In the $\text{La}_{1-x}\text{Sr}_x\text{Ni}_{0.5}\text{Cu}_{0.5}\text{O}_{3-\delta}$ ($x = 0$ and 0.05) oxides, the presence of strontium at the A-site led to a reduction in the unit cell volume and density, which was also observed in the series of $\text{La}_{1-x}\text{Sr}_x\text{Ni}_{0.75}\text{Cu}_{0.25}\text{O}_{3-\delta}$ ($x = 0, 0.05$ and 0.1) perovskites.

As presented in Figure 3, the microstructure studies of the $\text{La}_{1-x}\text{Sr}_x\text{Ni}_{0.75}\text{Cu}_{0.25}\text{O}_{3-\delta}$ ($x = 0, 0.05$ and 0.1) samples and $\text{La}_{1-x}\text{Sr}_x\text{Ni}_{0.5}\text{Cu}_{0.5}\text{O}_{3-\delta}$ ($x = 0$ and 0.05) powders show the presence of both small particles ($\leq 1 \mu\text{m}$) and larger aggregates (around $20 \mu\text{m}$). The grain size of the studied materials is smaller than $1 \mu\text{m}$, and all materials tend to form agglomerates, which results from the fact that forming agglomerates can reduce the large specific surface area of the small powders. For the studied powders, no correlation was found between the content of strontium and the particle size distribution of all the investigated materials.

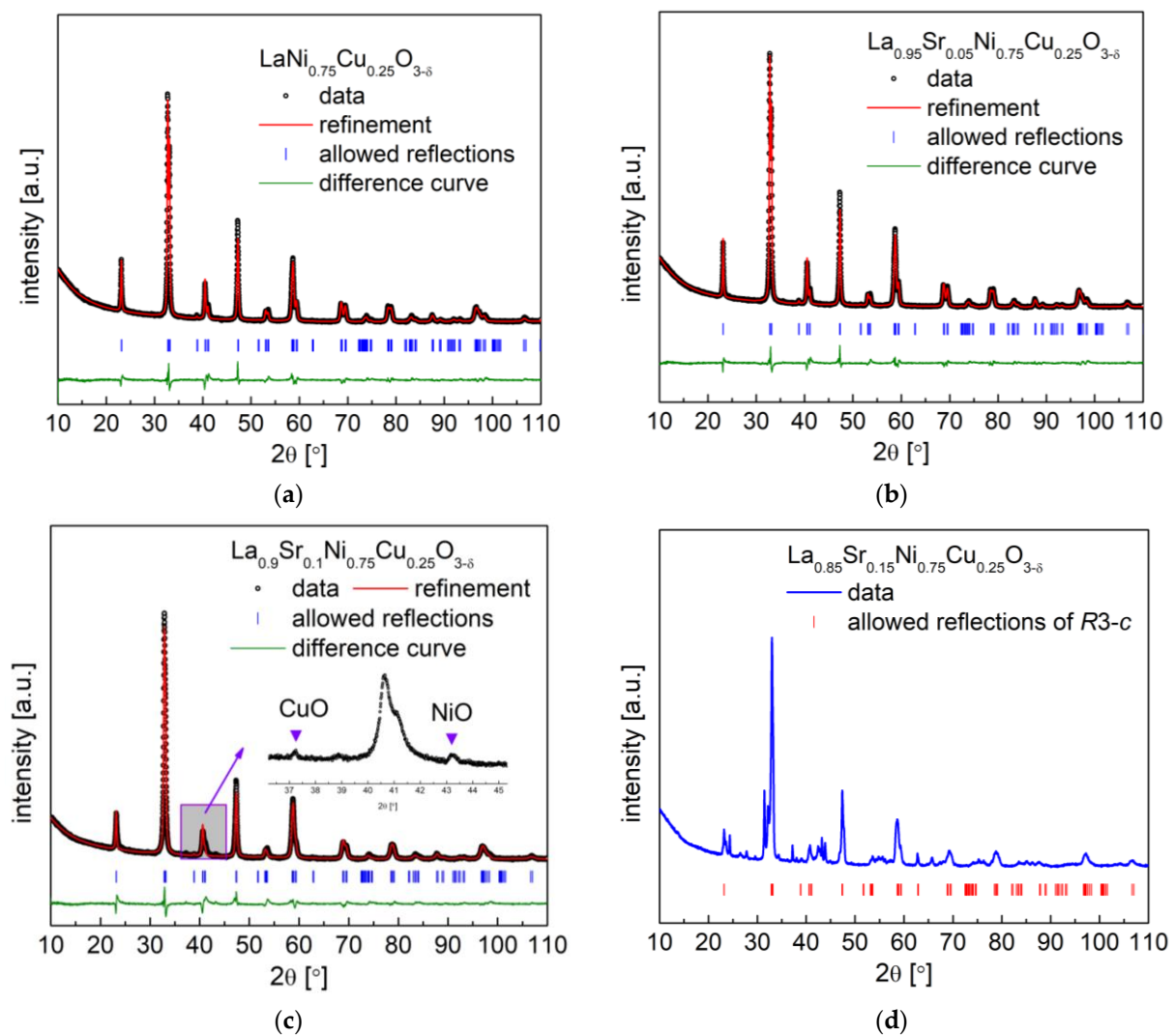


Figure 1. XRD patterns with Rietveld refinement recorded for $\text{La}_{1-x}\text{Sr}_x\text{Ni}_{0.75}\text{Cu}_{0.25}\text{O}_{3-\delta}$ oxides with (a) $x = 0$; (b) $x = 0.05$; (c) $x = 0.1$; (d) XRD patterns of $\text{La}_{0.85}\text{Sr}_{0.15}\text{Ni}_{0.75}\text{Cu}_{0.25}\text{O}_{3-\delta}$ oxides.

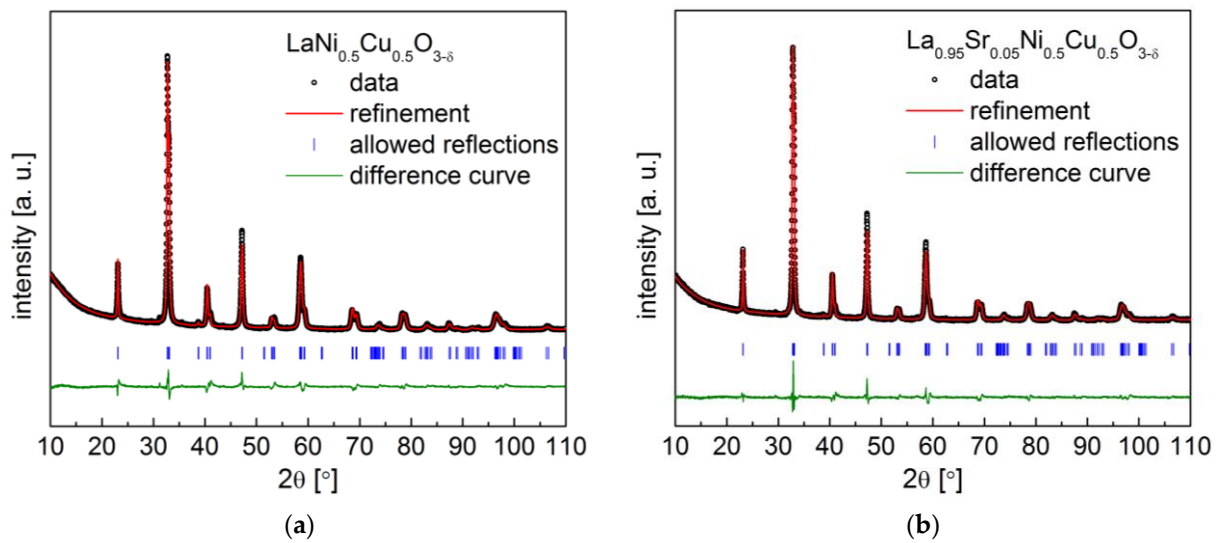


Figure 2. XRD patterns with Rietveld refinement recorded for $\text{La}_{1-x}\text{Sr}_x\text{Ni}_{0.5}\text{Cu}_{0.5}\text{O}_{3-\delta}$ oxides with (a) $x = 0$; (b) $x = 0.05$.

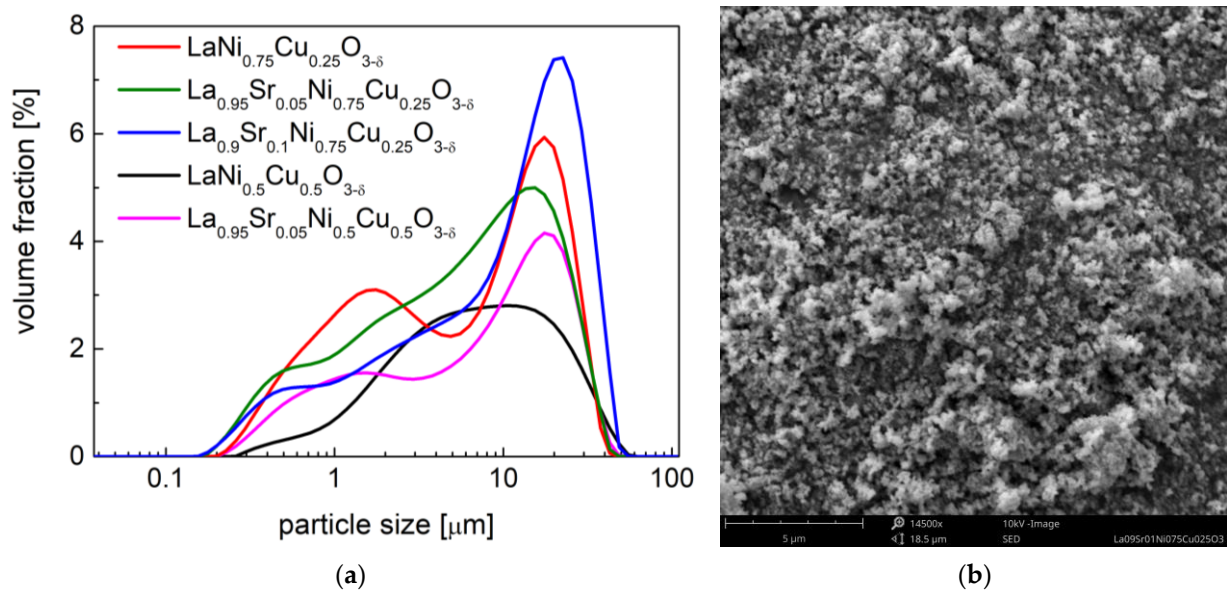


Figure 3. (a) Particle size analysis results of $\text{La}_{1-x}\text{Sr}_x\text{Ni}_{1-y}\text{Cu}_y\text{O}_{3-\delta}$ powders; (b) exemplary scanning electron micrograph of $\text{La}_{0.9}\text{Sr}_{0.1}\text{Ni}_{0.75}\text{Cu}_{0.25}\text{O}_{3-\delta}$ perovskite.

The high-temperature XRD studies conducted between 25 °C and 800 °C in air (data recorded during cooling) presented ongoing crystal structural changes in the studied samples (Figures 4 and 5). All investigated materials at high temperatures presented a regular simple perovskite structure with the $Pm-3m$ space group. The continuous phase transition from $R-3c$ ($a^- a^- a^-$) to $Pm-3m$ ($a^0 a^0 a^0$) in materials was characterized by the second order. The phase transition from $R-3c$ to the $Pm-3m$ regular one was related to the fact that the rotation angle of the BO_6 octahedra continually decreases with the temperature (during heating) until it reaches zero.

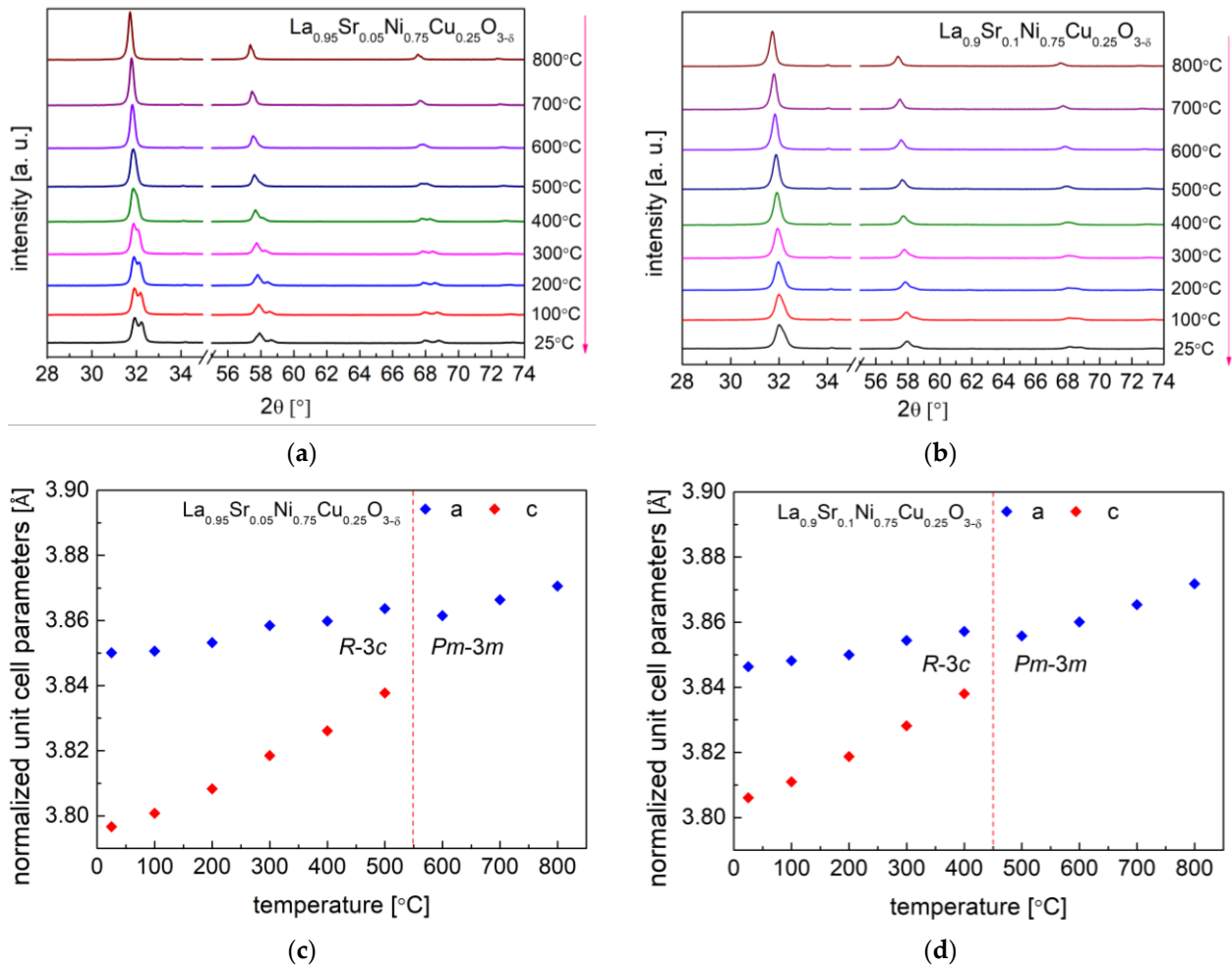


Figure 4. HT-XRD diffractograms recorded during the cooling from 800 °C to 25 °C in air for: (a) $\text{La}_{0.95}\text{Sr}_{0.05}\text{Ni}_{0.75}\text{Cu}_{0.25}\text{O}_{3-\delta}$ and (b) $\text{La}_{0.9}\text{Sr}_{0.1}\text{Ni}_{0.75}\text{Cu}_{0.25}\text{O}_{3-\delta}$; Normalized unit cell parameters dependence on temperature for (c) $\text{La}_{0.95}\text{Sr}_{0.05}\text{Ni}_{0.75}\text{Cu}_{0.25}\text{O}_{3-\delta}$ and (d) $\text{La}_{0.9}\text{Sr}_{0.1}\text{Ni}_{0.75}\text{Cu}_{0.25}\text{O}_{3-\delta}$.

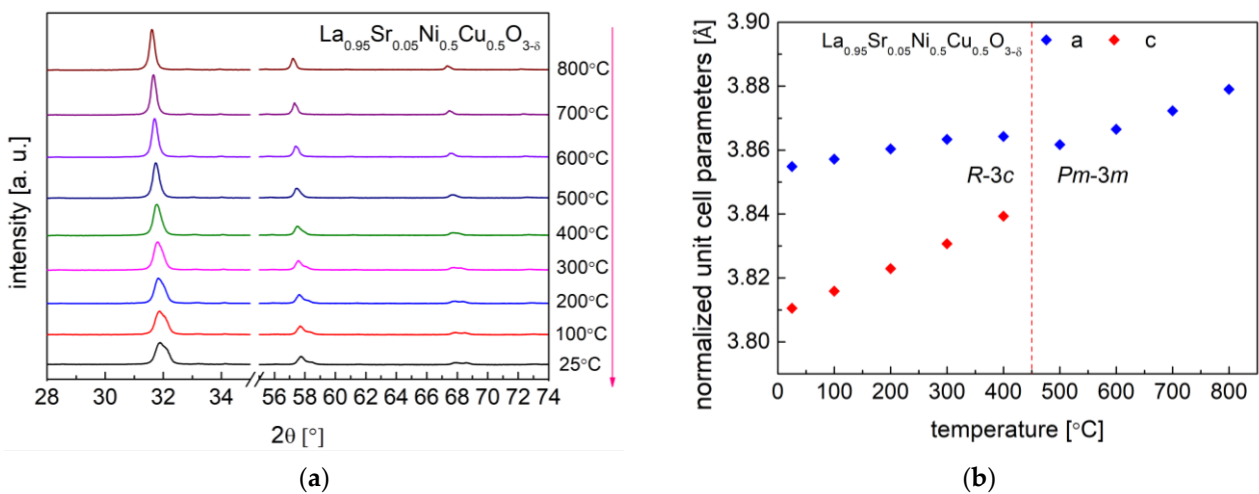


Figure 5. (a) HT-XRD diffractograms recorded for $\text{La}_{0.95}\text{Sr}_{0.05}\text{Ni}_{0.5}\text{Cu}_{0.5}\text{O}_{3-\delta}$; (b) Normalized unit cell parameters dependence on temperature for $\text{La}_{0.95}\text{Sr}_{0.05}\text{Ni}_{0.5}\text{Cu}_{0.5}\text{O}_{3-\delta}$.

A similar phase transition behavior was recorded for the $\text{LaNi}_{0.75}\text{Cu}_{0.25}\text{O}_{3-\delta}$ and $\text{LaNi}_{0.5}\text{Cu}_{0.5}\text{O}_{3-\delta}$ samples in our previous work [40]. For the series of $\text{La}_{1-x}\text{Sr}_x\text{Ni}_{0.75}\text{Cu}_{0.25}\text{O}_{3-\delta}$

($x = 0.05$ and 0.1) materials, the phase transition temperature was recorded at $550\text{ }^{\circ}\text{C}$ and $450\text{ }^{\circ}\text{C}$, respectively, as shown in Figure 4. A similar situation is present for the $\text{La}_{0.95}\text{Sr}_{0.05}\text{Ni}_{0.5}\text{Cu}_{0.5}\text{O}_{3-\delta}$ oxide in Figure 5, and the phase transition occurred between $400\text{ }^{\circ}\text{C}$ and $500\text{ }^{\circ}\text{C}$. As shown in Table 2, the increase in strontium content in the investigated samples decreased the phase transition temperature. It was also reported that, in the LaCrO_3 system, the substitution of La with Sr also lowers the phase transition temperature (between *Pbnm* orthorhombic and *R-3c* rhombohedral structures) [53,54]. Interestingly, the $\text{La}_{0.95}\text{Sr}_{0.05}\text{Ni}_{0.5}\text{Cu}_{0.5}\text{O}_{3-\delta}$ perovskite had the lowest phase transition temperature ($450\text{ }^{\circ}\text{C}$) among all the studied materials, while $\text{LaNi}_{0.75}\text{Cu}_{0.25}\text{O}_{3-\delta}$ showed the highest phase transition temperature ($850\text{ }^{\circ}\text{C}$). The phase transition of all the studied materials did not proceed monotonously, as evidenced by the behavior of the normalized unit cell *c* parameter, which is strongly related to the evolution of oxygen content recorded in the following TG measurements.

Table 2. Phase transition temperature of $\text{La}_{1-x}\text{Sr}_x\text{Ni}_{1-y}\text{Cu}_y\text{O}_{3-\delta}$ oxides determined from high-temperature XRD studies in air.

| Sample | Phase Transition Temperature |
|---|------------------------------------|
| $\text{LaNi}_{0.75}\text{Cu}_{0.25}\text{O}_{3-\delta}$ | $850\text{ }^{\circ}\text{C}$ [40] |
| $\text{La}_{0.95}\text{Sr}_{0.05}\text{Ni}_{0.75}\text{Cu}_{0.25}\text{O}_{3-\delta}$ | $550\text{ }^{\circ}\text{C}$ |
| $\text{La}_{0.9}\text{Sr}_{0.1}\text{Ni}_{0.75}\text{Cu}_{0.25}\text{O}_{3-\delta}$ | $450\text{ }^{\circ}\text{C}$ |
| $\text{LaNi}_{0.5}\text{Cu}_{0.5}\text{O}_{3-\delta}$ | $750\text{ }^{\circ}\text{C}$ [40] |
| $\text{La}_{0.95}\text{Sr}_{0.05}\text{Ni}_{0.5}\text{Cu}_{0.5}\text{O}_{3-\delta}$ | $450\text{ }^{\circ}\text{C}$ |

3.2. Thermal Expansion Properties and Oxygen Content

The above-presented data collected from the HT-XRD studies also yielded the unit cell volume ($V^{1/3}$) as a function of temperature, as shown in Figure 6. With the gained characteristics, it was possible to establish a thermal expansion coefficient based on the relative unit cell volume ($V^{1/3}$) changes, and the TEC results are presented in Table 3. In general, for all the studied samples, two linear expansion behaviors with different TEC values were recorded, which is related to the phase transition and oxygen release from the material (chemical expansion effect). Similar characteristics were also observed in the dilatometry measurements, which are shown in Figure 7. The small differences between the TEC values obtained from the dilatometry measurements and calculated from the HT-XRD data are shown in Table 3, which could be associated with some of porosity in the sinters in the dilatometry measurements and the different kinetics of the phase transition in the sinters and powder. Generally, the increase in strontium content in materials increases average TEC values, which is advantageous. However, Sr doping positively contributes to the generation of oxygen vacancies in materials, thus favoring ionic transport (see the following studies). The main/significant thermal expansion contribution is from the high temperature range (linked with the chemical expansion).

Table 3. Thermal expansion coefficients [10^{-6} K^{-1}] of $\text{La}_{1-x}\text{Sr}_x\text{Ni}_{1-y}\text{Cu}_y\text{O}_{3-\delta}$ samples from dilatometry studies and high-temperature XRD measurements in air.

| | HT-XRD (25–400/500 °C) | HT-XRD (500–800 °C) | Dilatometry (25–400 °C) | Dilatometry (550–800 °C) | HT-XRD (25–800 °C) | Dilatometry (25–800 °C) |
|---|---------------------------|------------------------|----------------------------|-----------------------------|-----------------------|----------------------------|
| $\text{LaNi}_{0.75}\text{Cu}_{0.25}\text{O}_{3-\delta}$ | - | - | 11.1 | 15.0 | - | 14.3 |
| $\text{La}_{0.95}\text{Sr}_{0.05}\text{Ni}_{0.75}\text{Cu}_{0.25}\text{O}_{3-\delta}$ | 12.8 | 11.8 | 11.1 | 15.4 | 12.7 | 14.6 |
| $\text{La}_{0.9}\text{Sr}_{0.1}\text{Ni}_{0.75}\text{Cu}_{0.25}\text{O}_{3-\delta}$ | 12.5 | 13.9 | 11.1 | 15.8 | 13.2 | 15.1 |
| $\text{LaNi}_{0.5}\text{Cu}_{0.5}\text{O}_{3-\delta}$ | - | - | 11.1 | 15.0 | - | 13.9 |
| $\text{La}_{0.95}\text{Sr}_{0.05}\text{Ni}_{0.5}\text{Cu}_{0.5}\text{O}_{3-\delta}$ | 11.2 | 15.1 | 11.5 | 15.2 | 12.9 | 14.1 |

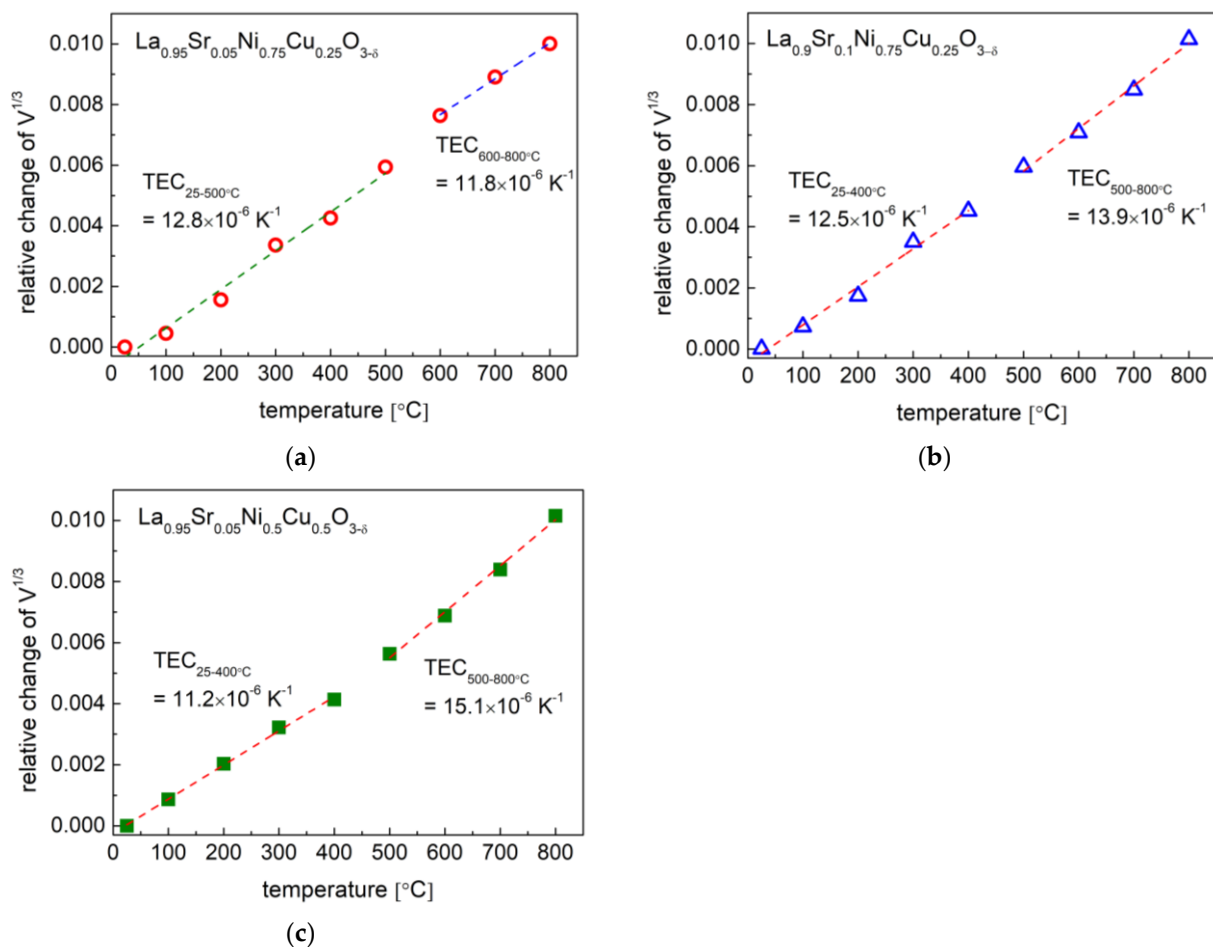


Figure 6. Thermal expansion coefficients calculated from HT-XRD data ($V^{1/3}$) for (a) $\text{La}_{0.95}\text{Sr}_{0.05}\text{Ni}_{0.75}\text{Cu}_{0.25}\text{O}_{3-\delta}$; (b) $\text{La}_{0.9}\text{Sr}_{0.1}\text{Ni}_{0.75}\text{Cu}_{0.25}\text{O}_{3-\delta}$; (c) $\text{La}_{0.95}\text{Sr}_{0.05}\text{Ni}_{0.5}\text{Cu}_{0.5}\text{O}_{3-\delta}$.

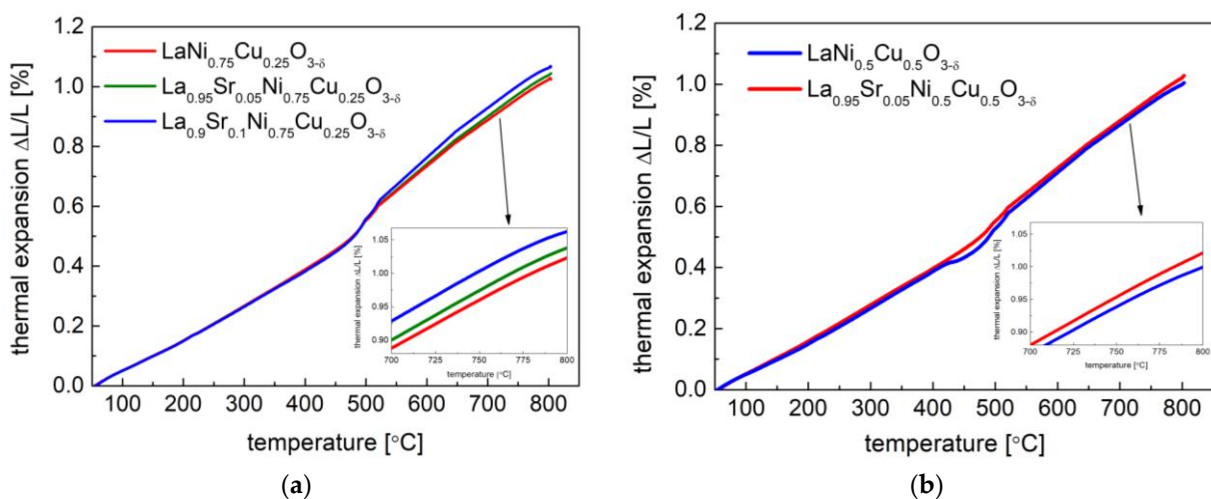


Figure 7. Thermal expansion behavior of (a) $\text{La}_{1-x}\text{Sr}_x\text{Ni}_{0.75}\text{Cu}_{0.25}\text{O}_{3-\delta}$ ($x = 0, 0.05$ and 0.1) samples; (b) $\text{La}_{1-x}\text{Sr}_x\text{Ni}_{0.5}\text{Cu}_{0.5}\text{O}_{3-\delta}$ ($x = 0$ and 0.05) sinters by dilatometry measurements.

The average TEC values calculated for all the samples in temperatures between 25°C and 800°C ranged from $13.9 \times 10^{-6} \text{K}^{-1}$ to $15.1 \times 10^{-6} \text{K}^{-1}$. The measured TEC values were moderate and comparable to Ni- and Cu-containing perovskites and perovskite-related oxides, including the following: $\text{La}_{1.5}\text{Ba}_{1.5}\text{Cu}_3\text{O}_{7\pm\delta}$ — $15.5 \times 10^{-6} \text{K}^{-1}$ [28];

$\text{LaNi}_{0.75}\text{Cu}_{0.25}\text{O}_{3-\delta}$ — $13.7 \times 10^{-6} \text{ K}^{-1}$ [40]; $\text{LaNi}_{0.5}\text{Cu}_{0.5}\text{O}_{3-\delta}$ — $14.5 \times 10^{-6} \text{ K}^{-1}$ [40]; $\text{PrNiO}_{3-\delta}$ — $12.7 \times 10^{-6} \text{ K}^{-1}$ [55]; $\text{Pr}_2\text{CuO}_{4+\delta}$ — $13.0 \times 10^{-6} \text{ K}^{-1}$ [56]; $\text{Pr}_2\text{Ni}_{0.5}\text{Cu}_{0.5}\text{O}_{4+\delta}$ — $12.7 \times 10^{-6} \text{ K}^{-1}$ [34]; and $\text{La}_2\text{Ni}_{0.5}\text{Cu}_{0.5}\text{O}_{4+\delta}$ — $13.9 \times 10^{-6} \text{ K}^{-1}$ [34] or $12.8 \times 10^{-6} \text{ K}^{-1}$ [33]. The recorded TEC values for the $\text{La}_{1-x}\text{Sr}_x\text{Ni}_{1-y}\text{Cu}_y\text{O}_{3-\delta}$ oxides were also close to the TECs of commonly used electrolytes, including $\text{La}_{0.9}\text{Sr}_{0.1}\text{Ga}_{0.8}\text{Mg}_{0.2}\text{O}_{3-\delta}$ — $12.17 \times 10^{-6} \text{ K}^{-1}$, $\text{Zr}_{0.85}\text{Y}_{0.15}\text{O}_{2-\delta}$ — $10.8 \times 10^{-6} \text{ K}^{-1}$, and $\text{Ce}_{0.8}\text{Gd}_{0.2}\text{O}_{2-\delta}$ — $12.5 \times 10^{-6} \text{ K}^{-1}$ [57] (contrary to the co-containing samples [24,58]). Therefore, the delamination problem due to the TEC mismatch was alleviated, thus yielding a stable SOFC performance with the considered cathode materials.

The oxygen content of the $\text{La}_{1-x}\text{Sr}_x\text{Ni}_{0.75}\text{Cu}_{0.25}\text{O}_{3-\delta}$ ($x = 0, 0.05$ and 0.1) and $\text{La}_{1-x}\text{Sr}_x\text{Ni}_{0.5}\text{Cu}_{0.5}\text{O}_{3-\delta}$ ($x = 0$ and 0.05) materials at room temperature was determined by the iodometric titration. The oxygen content change as a function of temperature is recorded in Figure 8, and the average oxidation state of B-site cations in the studied compounds at RT are presented in Table 4. In general, the increase in strontium doping at the A-site contributes to an increase in oxygen vacancies, thus decreasing the oxygen content in materials. The favorable Sr-doping effect on the formation of oxygen vacancies has also been observed in $\text{La}_{1-x}\text{Sr}_x\text{MO}_{3-\delta}$ ($M = \text{Fe}, \text{Mn}$) perovskites [44].

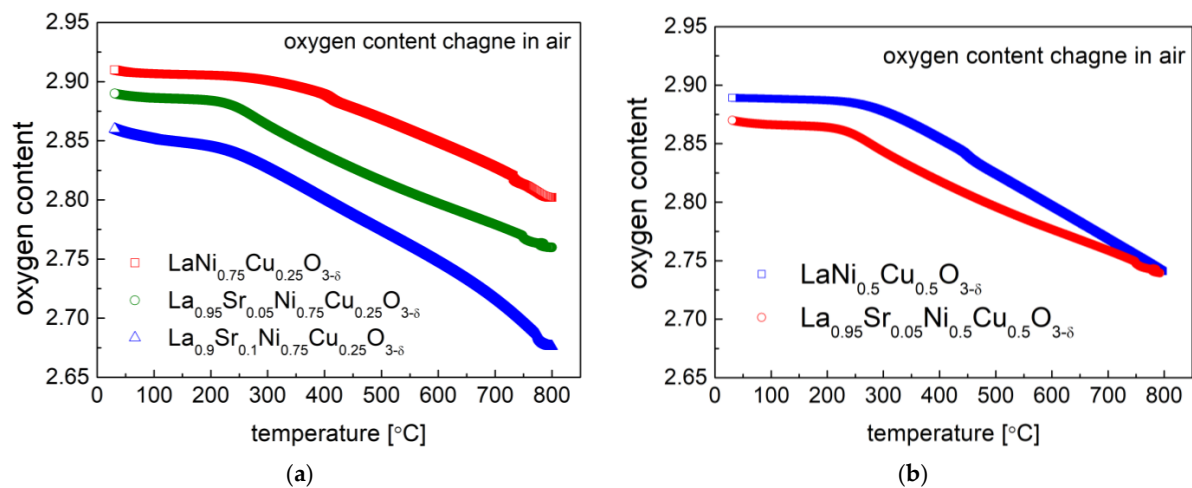


Figure 8. Oxygen content evolution in air for (a) $\text{La}_{1-x}\text{Sr}_x\text{Ni}_{0.75}\text{Cu}_{0.25}\text{O}_{3-\delta}$ ($x = 0, 0.05$ and 0.1); (b) $\text{La}_{1-x}\text{Sr}_x\text{Ni}_{0.5}\text{Cu}_{0.5}\text{O}_{3-\delta}$ ($x = 0$ and 0.05) oxides.

Table 4. Oxygen content and average oxidation state of B-site cations in studied compounds.

| | Average Oxidation State of B-Site Cations Cu/Ni at RT | Oxygen Content at RT | Oxygen Content at 600 °C |
|---|---|----------------------|--------------------------|
| $\text{LaNi}_{0.75}\text{Cu}_{0.25}\text{O}_{3-\delta}$ | 2.82 | 2.91 | 2.85 |
| $\text{La}_{0.95}\text{Sr}_{0.05}\text{Ni}_{0.75}\text{Cu}_{0.25}\text{O}_{3-\delta}$ | 2.83 | 2.89 | 2.80 |
| $\text{La}_{0.9}\text{Sr}_{0.1}\text{Ni}_{0.75}\text{Cu}_{0.25}\text{O}_{3-\delta}$ | 2.83 | 2.86 | 2.75 |
| $\text{LaNi}_{0.5}\text{Cu}_{0.5}\text{O}_{3-\delta}$ | 2.78 | 2.89 | 2.80 |
| $\text{La}_{0.95}\text{Sr}_{0.05}\text{Ni}_{0.5}\text{Cu}_{0.5}\text{O}_{3-\delta}$ | 2.79 | 2.87 | 2.78 |

The substitution of La with Sr also led to an increase in the average oxidation state of B-site cations (Ni and Cu), causing a reduction in the unit cell volume of the studied materials (recorded in Table 1). The presence of the mixture of +3 and +2 oxidation states for Ni/Cu in $\text{La}_{1-x}\text{Sr}_x\text{Ni}_{1-y}\text{Cu}_y\text{O}_{3-\delta}$ should benefit the electronic charge transfer in materials. In the high-temperature range and in materials, additional oxygen vacancies were generated according to the following reaction: $\text{O}_\text{O}^\times \leftrightarrow 1/2\text{O}_2 + \text{V}_\text{O}^{\bullet\bullet} + 2\text{e}^-$. A significant mass drop was observed for all samples above 250 °C, related to the oxygen release from the lattice.

Interestingly, the $\text{La}_{0.9}\text{Sr}_{0.1}\text{Ni}_{0.75}\text{Cu}_{0.25}\text{O}_{3-\delta}$ compound exhibited the highest oxygen non-stoichiometry at RT ($\delta = 0.14$) and 600 °C ($\delta = 0.25$) among all the studied materials.

3.3. Stability and Compatibility with Solid Electrolytes

The chemical stability and compatibility of electrode materials with applied solid electrolytes are crucial for the stable and long-term performance of SOFCs. Long-term chemical and thermal stability studies of analyzed $\text{La}_{1-x}\text{Sr}_x\text{Ni}_{1-y}\text{Cu}_y\text{O}_{3-\delta}$ versus mostly used solid electrolytes, including CGO10, LSGM, and 8YSZ electrolytes, were conducted in air at 800 °C for 100 h. As can be observed in Figure 9, no reactivity was observed, with both the cathode materials and CGO10 phases being virtually unchanged. All studied $\text{La}_{1-x}\text{Sr}_x\text{Ni}_{1-y}\text{Cu}_y\text{O}_{3-\delta}$ cathode materials were stable and compatible with used CGO10. On the contrary, for $\text{La}_{1-x}\text{Sr}_x\text{Ni}_{1-y}\text{Cu}_y\text{O}_{3-\delta}$, some reactivity was visible towards LSGM with the emergence of additional unidentified peaks (see Figure 10), especially for the $\text{La}_{1-x}\text{Sr}_x\text{Ni}_{0.5}\text{Cu}_{0.5}\text{O}_{3-\delta}$ ($x = 0$ and 0.05) materials.

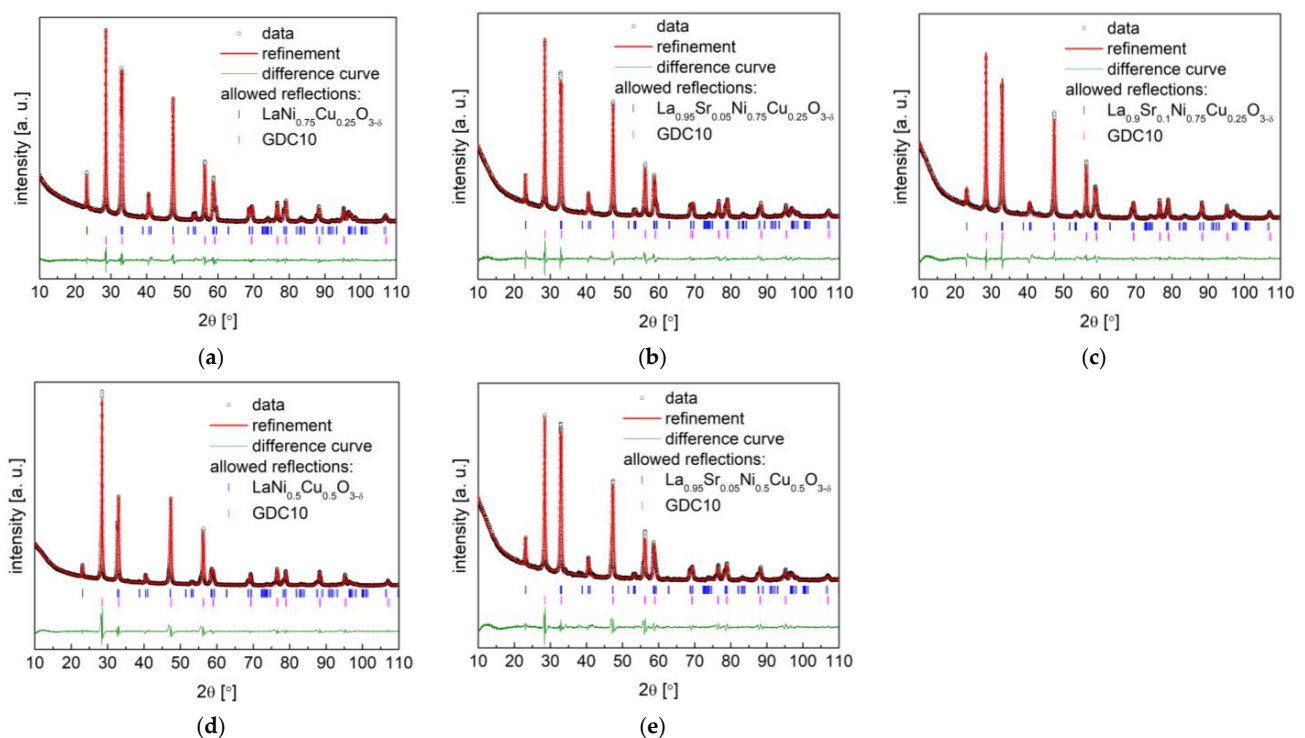


Figure 9. XRD diffractograms with Rietveld refinement of (a) $\text{LaNi}_{0.75}\text{Cu}_{0.25}\text{O}_{3-\delta}$; (b) $\text{La}_{0.95}\text{Sr}_{0.05}\text{Ni}_{0.75}\text{Cu}_{0.25}\text{O}_{3-\delta}$; (c) $\text{La}_{0.9}\text{Sr}_{0.1}\text{Ni}_{0.75}\text{Cu}_{0.25}\text{O}_{3-\delta}$; (d) $\text{LaNi}_{0.5}\text{Cu}_{0.5}\text{O}_{3-\delta}$; (e) $\text{La}_{0.95}\text{Sr}_{0.05}\text{Ni}_{0.5}\text{Cu}_{0.5}\text{O}_{3-\delta}$ with $\text{Ce}_{0.9}\text{Gd}_{0.1}\text{O}_{1.95}$ electrolyte after annealing at 800 °C for 100 h.

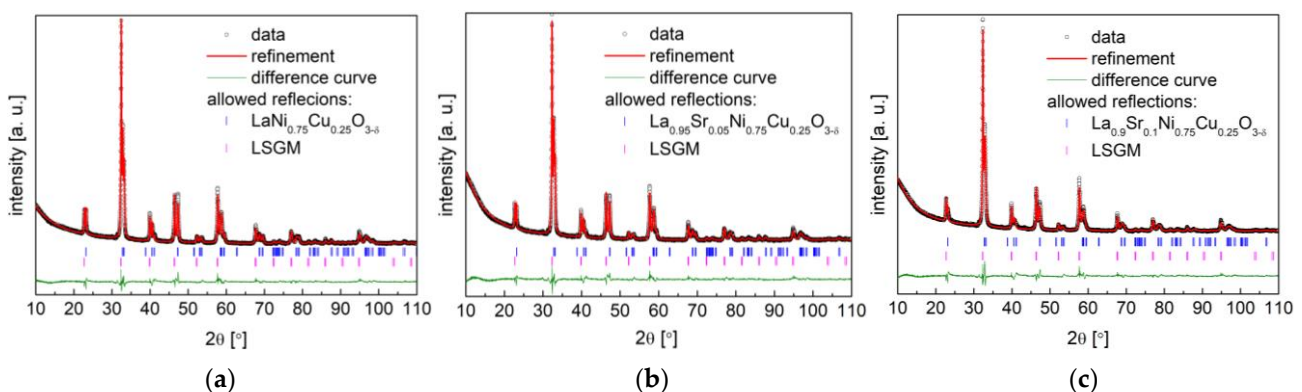


Figure 10. Cont.

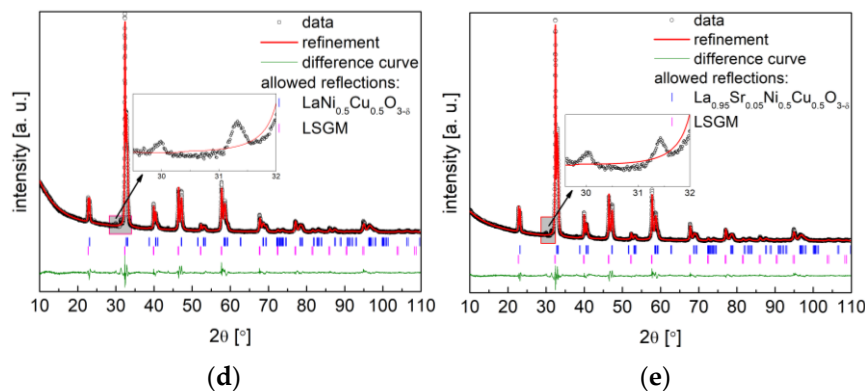


Figure 10. XRD diffractograms with Rietveld refinement of (a) $\text{LaNi}_{0.75}\text{Cu}_{0.25}\text{O}_{3-\delta}$; (b) $\text{La}_{0.95}\text{Sr}_{0.05}\text{Ni}_{0.75}\text{Cu}_{0.25}\text{O}_{3-\delta}$; (c) $\text{La}_{0.9}\text{Sr}_{0.1}\text{Ni}_{0.75}\text{Cu}_{0.25}\text{O}_{3-\delta}$; (d) $\text{LaNi}_{0.5}\text{Cu}_{0.5}\text{O}_{3-\delta}$; (e) $\text{La}_{0.95}\text{Sr}_{0.05}\text{Ni}_{0.5}\text{Cu}_{0.5}\text{O}_{3-\delta}$ with LSGM solid electrolyte after annealing in air at 800 °C for 100 h.

Unfortunately, in the case of $\text{La}_{1-x}\text{Sr}_x\text{Ni}_{1-y}\text{Cu}_y\text{O}_{3-\delta}$ with the 8YSZ electrolyte (Figure 11), the considered cathode materials were not compatible with the studied electrolyte, presenting evident additional peaks, which limited the direct contact of the $\text{La}_{1-x}\text{Sr}_x\text{Ni}_{1-y}\text{Cu}_y\text{O}_{3-\delta}$ materials with 8YSZ in SOFCs. Therefore, for the anode-supported SOFC (Ni-8YSZ | 8YSZ | CGO10 | cathode) studied in the following section, a CGO10 buffer layer was applied to ensure a good and stable cell performance.

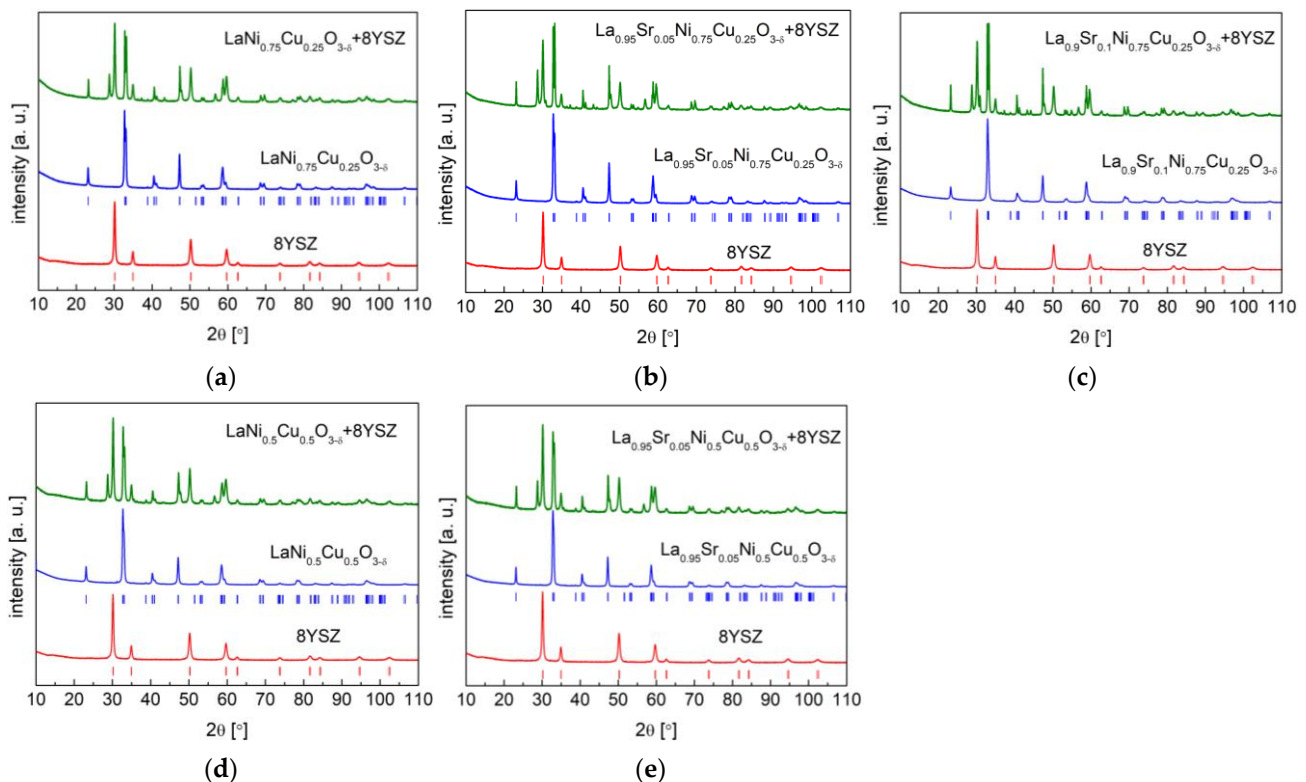


Figure 11. XRD diffractograms of (a) $\text{LaNi}_{0.75}\text{Cu}_{0.25}\text{O}_{3-\delta}$; (b) $\text{La}_{0.95}\text{Sr}_{0.05}\text{Ni}_{0.75}\text{Cu}_{0.25}\text{O}_{3-\delta}$; (c) $\text{La}_{0.9}\text{Sr}_{0.1}\text{Ni}_{0.75}\text{Cu}_{0.25}\text{O}_{3-\delta}$; (d) $\text{LaNi}_{0.5}\text{Cu}_{0.5}\text{O}_{3-\delta}$; (e) $\text{La}_{0.95}\text{Sr}_{0.05}\text{Ni}_{0.5}\text{Cu}_{0.5}\text{O}_{3-\delta}$ with 8YSZ solid electrolyte after annealing in air at 800 °C for 100 h.

3.4. Electrochemical Performance of IT-SOFC with $\text{La}_{0.95}\text{Sr}_{0.05}\text{Ni}_{0.5}\text{Cu}_{0.5}\text{O}_{3-\delta}$

A Cu-content $\text{La}_{0.95}\text{Sr}_{0.05}\text{Ni}_{0.5}\text{Cu}_{0.5}\text{O}_{3-\delta}$ oxide with low TEC ($14.1 \times 10^{-6} \text{ K}^{-1}$) and high oxygen non-stoichiometry ($\delta = 0.22$ at 600 °C) was selected as a cathode material for the IT-SOFC, working at around 600 °C (see Figure 12). The scanning electron mi-

crograph of $\text{La}_{0.95}\text{Sr}_{0.05}\text{Ni}_{0.5}\text{Cu}_{0.5}\text{O}_{3-\delta}$ powder applied in the cathode layer is presented in Figure 13, which shows a small grain size ($\leq 1 \mu\text{m}$). It is worth emphasizing that the $\text{La}_{0.95}\text{Sr}_{0.05}\text{Ni}_{0.5}\text{Cu}_{0.5}\text{O}_{3-\delta}$ cathode layer was sintered at a relatively low temperature (at only $800 \text{ }^\circ\text{C}$), yielding the cell fabrication process as facile and less energy-consuming, which can be related to the good sinterability of copper-containing materials and the well-attached cathode layer to CGO10 in the selected conditions.

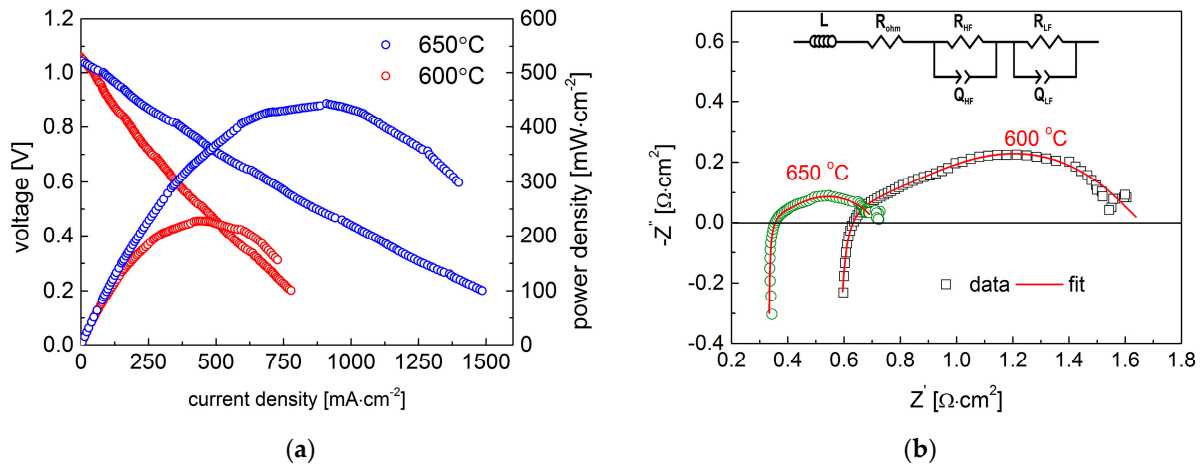


Figure 12. (a) Voltage and power density as a function of current density and (b) impedance spectra for anode-supported SOFC with $\text{La}_{0.95}\text{Sr}_{0.05}\text{Ni}_{0.5}\text{Cu}_{0.5}\text{O}_{3-\delta}$ -based cathode.

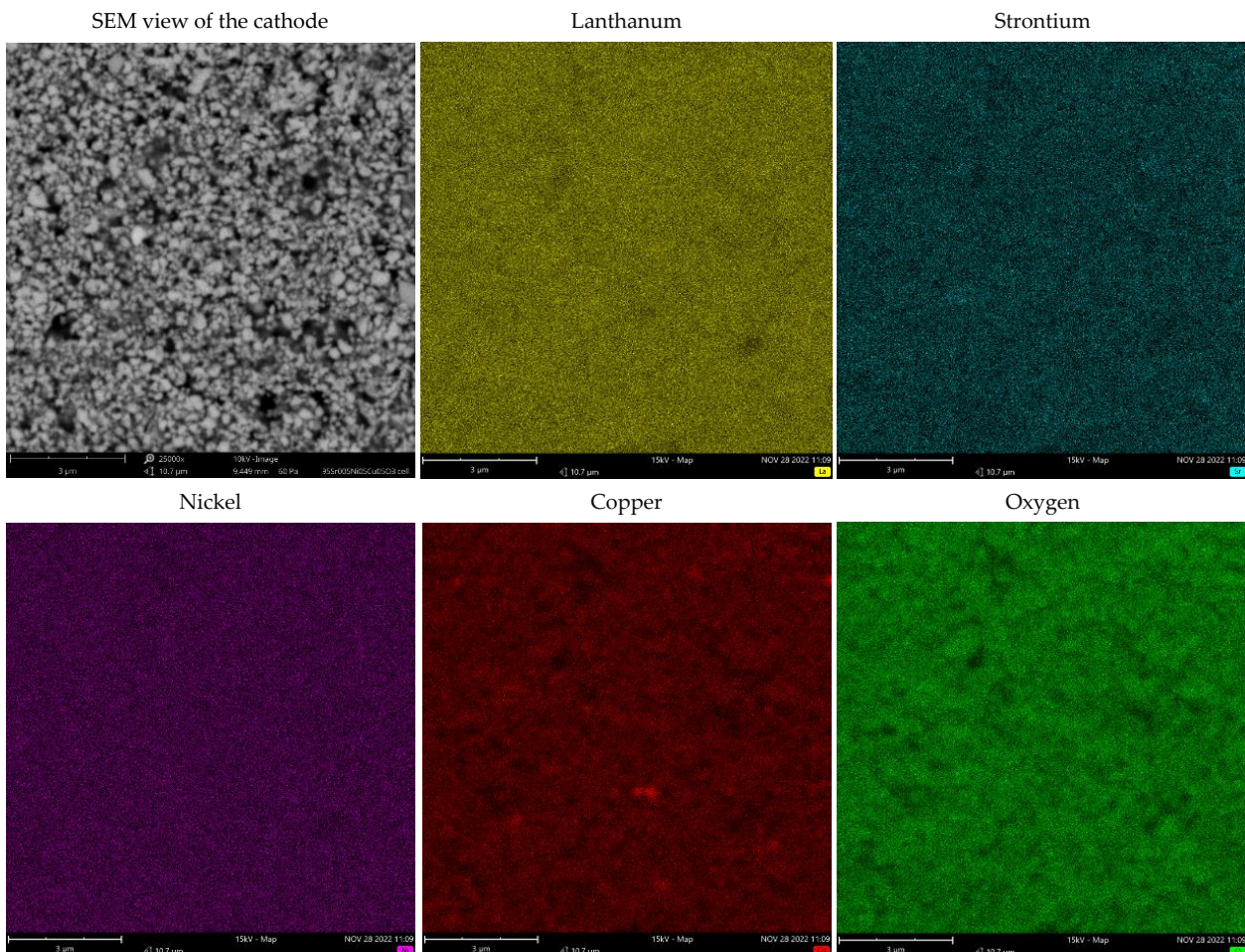


Figure 13. EDS map of element distribution in the $\text{La}_{0.95}\text{Sr}_{0.05}\text{Ni}_{0.5}\text{Cu}_{0.5}\text{O}_{3-\delta}$ cathode after cell tests.

The recorded SOFC voltage and power outputs as a function of the current density for the studied Ni-8YSZ | 8YSZ | CGO10 | La_{0.95}Sr_{0.05}Ni_{0.5}Cu_{0.5}O_{3-δ} cell are shown in Figure 12a. As can be observed, the maximum power yields reached very high values of approx. 450 mW·cm⁻² and 230 mW·cm⁻² in humidified hydrogen at 650 °C and 600 °C, respectively. Analyzing the shape of the voltage curves in Figure 12a, no obvious influence of activation polarization component can be observed, indicating a potential further improvement in SOFC performance. As can be seen in Table 5, the recorded power value for IT-SOFC with a La_{0.95}Sr_{0.05}Ni_{0.5}Cu_{0.5}O_{3-δ} cathode belongs to one of the best SOFC power outputs at the intermediate-temperature range, which is very encouraging.

The EIS spectra measured for the tested IT-SOFCs are presented in Nyquist plots in Figure 12b. The measured spectra consist of two semi-arcs, in which a high frequency arc can be connected with processes taking place on the electrode and electrolyte interface (e.g., charge transfer). Additionally, a low frequency arc is associated with the electrode surface reaction, including the adsorption and dissociation of molecular oxygen [50,59]. At 600 °C, the polarization related to high frequency ($R_{HF} = 0.625 \Omega \cdot \text{cm}^2$) dominated. The values recorded for the ohmic polarization and low frequency polarization were $R_{ohm} = 0.547 \Omega \cdot \text{cm}^2$ and $R_{LF} = 0.491 \Omega \cdot \text{cm}^2$, respectively. Meanwhile, at 650 °C, the electrode-related polarization ($R_p = R_{HF} + R_{LF} = 0.384 \Omega \cdot \text{cm}^2$) was comparable to ohmic polarization ($R_{ohm} = 0.330 \Omega \cdot \text{cm}^2$), which indicates the possibility of further improvement in cell performance.

Table 5. The crystal structure, thermal expansion coefficient, compatibility with electrolytes, and SOFC performance with selected cathode materials.

| Cathode Material | Crystal Structure | TEC [$\times 10^{-6} \text{ K}^{-1}$] | Towards Electrolyte | Cell Performance [mW·cm ⁻²] | Ref. |
|--|-----------------------------|---|------------------------------------|--|------------|
| La _{0.95} Sr _{0.05} Ni _{0.5} Cu _{0.5} O _{3-δ} | R3-c | 14.1 | Stable with CGO10 | 450 at 650 °C, 230 at 600 °C in wet H ₂ | This work |
| LaNi _{0.5} Cu _{0.5} O _{3-δ} | R3-c | 14.5 | Stable with LSGM | 120 at 650 °C in wet H ₂ | [40] |
| La _{1.5} Ba _{1.5} Cu ₃ O _{7±δ} | P4/ <i>mmm</i> | 15.5 | Stable with LSGM | 162 at 600 °C, 250 at 650 °C in wet H ₂ | [28] |
| LaNiO ₃ | R-3c | 13.7 | Stable with CGO20 | 477 at 650 °C in wet H ₂ with LaNiO ₃ /GDC composite cathode | [51,60,61] |
| La _{0.54} Sr _{0.46} Fe _{0.80} Cu _{0.20} O _{3-δ} | Two tetragonal phases | - | - | 452 at 600 °C in H ₂ | [62] |
| LaNi _{0.6} Fe _{0.4} O _{3-δ} | R-3c | 14.5 | Stable with BZCY (below 700 °C) | 431 at 650 °C, 232 at 600 °C in wet H ₂ | [63,64] |
| La ₂ Ni _{0.5} Cu _{0.5} O _{4±δ} | <i>Fmmm</i> , <i>F4/mmm</i> | 12.8, 13.9 | Stable with CGO20 | - | [34,56] |
| Nd _{1.9} Ce _{0.1} CuO ₄ | <i>I4/mmm</i> | 11.17 | Stable with CGO | 283 at 700 °C in wet H ₂ | [65] |
| NdBa _{0.5} Sr _{0.5} Cu ₂ O _{5±δ} | <i>P4/mmm</i> | 14.6 | Stable with LSGM | 343 at 750 °C | [66] |
| PrNiO _{3-δ} | <i>Pnma</i> | 12.7 | Stable with CGO20 | - | [55] |
| Pr ₂ NiO _{4±δ} | <i>Fmmm</i> | - | Stable with CGO25 | 50 at 600 °C, 80 at 650 °C in dry H ₂ | [67] |
| Pr ₂ Ni _{0.5} Cu _{0.5} O _{4±δ} | <i>Bmab</i> | 12.7 | Stable with CGO20 | 35 at 650 °C in dry H ₂ | [34] |
| Pr ₂ CuO _{4±δ} | <i>I4/mmm</i> | 13.0 | Stable with CGO20 | 25 at 650 °C in dry H ₂ | [33] |
| Pr _{1.7} Ca _{0.3} NiO _{4±δ} | <i>Fmmm</i> | - | Stable with BCGCu | 96 at 650 °C, 61 at 600 °C in wet H ₂ | [68] |
| PrBa _{0.5} Sr _{0.5} Cu ₂ O _{5±δ} | <i>P4/mmm</i> | 14.2 | Stable with LSGM | 369 at 750 °C | [66] |
| (Pr _{0.5} Nd _{0.5}) _{0.7} Sr _{0.3} MnO _{3-δ} + SDC or 8YSZ (in molar ratio 3:2) | - | - | Stable with SDC and 8YSZ | 166 at 650 °C in wet H ₂ , 172 at 600 °C in wet H ₂ | [69,70] |
| Sr ₂ Fe _{1.2} Mg _{0.2} Mo _{0.6} O _{6-δ} | <i>Fm-3m</i> | 12.9-14.6 in air; 14.6-16.7 in 5% H ₂ | Stable with CGO20 | - | [71] |
| BaCe _{0.05} Fe _{0.95} O _{3-δ} | <i>Pm-3m</i> | - | Stable with SDC | 315 at 650 °C, 212 at 600 °C in wet H ₂ | [72] |

CGO10: Ce_{0.9}Gd_{0.1}O_{1.95}; CGO20: Ce_{0.8}Gd_{0.2}O_{1.9}; LSGM: La_{0.8}Sr_{0.2}Ga_{0.8}Mg_{0.2}O_{3-d}; CGO25: Ce_{0.75}Gd_{0.25}O_{1.875}; SDC: Sm_{0.2}Ce_{0.8}O_{1.95}; BCGCu: BaCe_{0.89}Gd_{0.1}Cu_{0.01}O_{3-d}; SDC: Sm_{0.2}Ce_{0.8}O_{1.95}; BZCY: Ba(Zr_{0.1}Ce_{0.7}Y_{0.2})O_{3-d}.

In general, the cell power output (in Table 5) was strongly related to the thicknesses of the electrolytes and the types of applied electrolytes. A direct and exact comparison of power

densities for different SOFCs is very difficult. Nevertheless, the power output of 450 mW cm^{-2} at $650 \text{ }^\circ\text{C}$ for the anode-supported SOFC with a $\text{La}_{0.95}\text{Sr}_{0.05}\text{Ni}_{0.5}\text{Cu}_{0.5}\text{O}_{3-\delta}$ cathode is still one of the best results, especially compared with reported results for anode-supported cells with a $\text{La}_{0.8}\text{Sr}_{0.2}\text{MnO}_3$ -YSZ composite cathode (261 mW cm^{-2} at $700 \text{ }^\circ\text{C}$) [47], LaNiO_3 /GDC composite cathode (477 mW cm^{-2} at $650 \text{ }^\circ\text{C}$) [61], $(\text{Pr}_{0.5}\text{Nd}_{0.5})_{0.7}\text{Sr}_{0.3}\text{MnO}_{3-\delta}$ -YSZ composite cathode (325 mW cm^{-2} at $700 \text{ }^\circ\text{C}$) [70], and $\text{BaCe}_{0.05}\text{Fe}_{0.95}\text{O}_{3-\delta}$ cathode (315 mW cm^{-2} at $650 \text{ }^\circ\text{C}$) [72].

The post-mortem analysis of the $\text{La}_{0.95}\text{Sr}_{0.05}\text{Ni}_{0.5}\text{Cu}_{0.5}\text{O}_{3-\delta}$ cathode was conducted after the cell performance investigation. The scanning electron micrograph of the $\text{La}_{0.95}\text{Sr}_{0.05}\text{Ni}_{0.5}\text{Cu}_{0.5}\text{O}_{3-\delta}$ cathode is shown in Figure 13. The $\text{La}_{0.95}\text{Sr}_{0.05}\text{Ni}_{0.5}\text{Cu}_{0.5}\text{O}_{3-\delta}$ cathode presented a desired porous microstructure, which was maintained after the cell measurements. Furthermore, the EDS mapping studies of element distribution presented the uniform distribution of the La, Sr, Ni, and Cu elements in the $\text{La}_{0.95}\text{Sr}_{0.05}\text{Ni}_{0.5}\text{Cu}_{0.5}\text{O}_{3-\delta}$ cathode. However, some Cu-enriched particles can be observed, which is due to the appearance of a very small amount of CuO in the synthesis.

The presented excellent electrochemical performance of fabricated anode-supported IT-SOFCs clearly shows the strontium doping in Cu-content $\text{La}_{1-x}\text{Sr}_x\text{Ni}_{1-y}\text{Cu}_y\text{O}_{3-\delta}$ perovskite oxides is a very effective strategy for the development of high-performance anode-supported SOFCs working at intermediate-temperature range.

4. Conclusions

Single-phase $\text{La}_{1-x}\text{Sr}_x\text{Ni}_{0.75}\text{Cu}_{0.25}\text{O}_{3-\delta}$ ($x = 0, 0.05$ and 0.1) and $\text{La}_{1-x}\text{Sr}_x\text{Ni}_{0.5}\text{Cu}_{0.5}\text{O}_{3-\delta}$ ($x = 0$ and 0.05) perovskites with strontium doping at the A-site have been successfully obtained using soft chemistry. The room-temperature crystal structure of all obtained $\text{La}_{1-x}\text{Sr}_x\text{Ni}_{1-y}\text{Cu}_y\text{O}_{3-\delta}$ compounds can be classified into the $R\bar{3}c$ trigonal system, and phase transitions from the $R\bar{3}c$ space group to a $Pm\bar{3}m$ simple perovskite have been recorded at a high-temperature range by HT-XRD studies. The substitution of La with Sr in the investigated materials decreased the phase transition temperature, and $\text{La}_{0.95}\text{Sr}_{0.05}\text{Ni}_{0.5}\text{Cu}_{0.5}\text{O}_{3-\delta}$ oxide presented the lowest phase transition temperature ($450 \text{ }^\circ\text{C}$) among all the considered materials. Strontium doping at the A-site significantly increased the oxygen non-stoichiometry and contributed to an increase in TEC values. The thermal expansion of the studied samples was found to be anisotropic, and the obtained TEC values are similar to the most commonly applied solid electrolytes (e.g., $14.1 \times 10^{-6} \text{ K}^{-1}$ for $\text{La}_{0.95}\text{Sr}_{0.05}\text{Ni}_{0.5}\text{Cu}_{0.5}\text{O}_{3-\delta}$).

All the investigated compounds are stable and chemically compatible with GDC-10 and have some reactivity with LSGM, while they are incompatible with the 8YSZ electrolyte. The selected $\text{La}_{0.95}\text{Sr}_{0.05}\text{Ni}_{0.5}\text{Cu}_{0.5}\text{O}_{3-\delta}$ perovskite was applied to fabricate full anode-supported IT-SOFCs, and a very good power yield was documented at $445 \text{ mW}\cdot\text{cm}^{-2}$ and $650 \text{ }^\circ\text{C}$ in humidified H_2 . The results indicate that studied perovskites with a strontium doping strategy can qualify as high-performance cathode materials for anode-supported SOFCs, yielding promising cell performance in the intermediate-temperature range (around $600 \text{ }^\circ\text{C}$).

Author Contributions: Conceptualization, investigation, methodology, visualization, J.L.; conceptualization, formal analysis, supervision, validation, writing—original draft preparation, K.Z.; providing anode-supported half-cells, review, R.K.; writing—review and editing, data analysis, A.N., H.Z. and M.C. All authors have read and agreed to the published version of the manuscript.

Funding: This project was funded by the National Science Centre, Poland, on the basis of the decision number UMO-2020/37/B/ST8/02097. K.Z. acknowledges financial support from AGH University of Science and Technology under grant no. 16.16.210.476.

Institutional Review Board Statement: Not applicable.

Informed Consent Statement: Not applicable.

Data Availability Statement: The data presented in this study are available on request from the corresponding author.

Conflicts of Interest: The authors declare no conflict of interest.

References

1. Boldrin, P.; Brandon, N.P. Progress and outlook for solid oxide fuel cells for transportation applications. *Nat. Catal.* **2019**, *2*, 571–577. [[CrossRef](#)]
2. Develos-Bagarinao, K.; Ishiyama, T.; Kishimoto, H.; Shimada, H.; Yamaji, K. Nanoengineering of cathode layers for solid oxide fuel cells to achieve superior power densities. *Nat. Commun.* **2021**, *12*, 3979. [[CrossRef](#)] [[PubMed](#)]
3. Park, S.; Vohs, J.M.; Gorte, R.J. Direct oxidation of hydrocarbons in a solid-oxide fuel cell. *Nature* **2000**, *404*, 265–267. [[CrossRef](#)] [[PubMed](#)]
4. Lenka, R.K.; Patro, P.K.; Patel, V.; Muhmood, L.; Mahata, T. Comparative investigation on the functional properties of alkaline earth metal (Ca, Ba, Sr) doped $\text{Nd}_2\text{NiO}_{4+\delta}$ oxygen electrode material for SOFC applications. *J. Alloy. Compd.* **2021**, *860*, 158490. [[CrossRef](#)]
5. Ding, H.; Tao, Z.; Liu, S.; Zhang, J. A High-Performing Sulfur-Tolerant and Redox-Stable Layered Perovskite Anode for Direct Hydrocarbon Solid Oxide Fuel Cells. *Sci. Rep.* **2015**, *5*, 18129. [[CrossRef](#)]
6. Brett, D.J.L.; Atkinson, A.; Brandon, N.P.; Skinner, S.J. Intermediate temperature solid oxide fuel cells. *Chem Soc. Rev.* **2008**, *37*, 1568–1578. [[CrossRef](#)] [[PubMed](#)]
7. Shao, Z.; Tadé, M.O. *Intermediate-Temperature Solid Oxide Fuel Cells: Materials and Applications*; Springer-Verlag: Berlin/Heidelberg, Germany, 2016.
8. Dong, Z.; Xia, T.; Li, Q.; Wang, J.; Li, S.; Sun, L.; Huo, L.; Zhao, H. Addressing the origin of highly catalytic activity of A-site Sr-doped perovskite cathodes for intermediate-temperature solid oxide fuel cells. *Electrochem. Commun.* **2022**, *140*, 107341. [[CrossRef](#)]
9. Xu, X.; Su, C.; Shao, Z. Fundamental Understanding and Application of $\text{Ba}_{0.5}\text{Sr}_{0.5}\text{Co}_{0.8}\text{Fe}_{0.2}\text{O}_{3-\delta}$ Perovskite in Energy Storage and Conversion: Past, Present, and Future. *Energy Fuels* **2021**, *35*, 13585–13609. [[CrossRef](#)]
10. Ndubuisi, A.; Abouali, S.; Singh, K.; Thangadurai, V. Recent advances, practical challenges, and perspectives of intermediate temperature solid oxide fuel cell cathodes. *J. Mater. Chem. A* **2022**, *10*, 2196–2227. [[CrossRef](#)]
11. Kumar, R.V.; Khandale, A.P. A review on recent progress and selection of cobalt-based cathode materials for low temperature-solid oxide fuel cells. *Renew. Sustain. Energy Rev.* **2022**, *156*, 111985. [[CrossRef](#)]
12. Liu, B.; Zhang, Y.; Zhang, L. Cathode for solid oxide fuel cell. *Int. J. Hydrog. Energy* **2009**, *34*, 1008–1014. [[CrossRef](#)]
13. Tietz, F.; Arul Raj, I.; Zahid, M.; Stöver, D. Electrical conductivity and thermal expansion of $\text{La}_{0.8}\text{Sr}_{0.2}(\text{Mn,Fe,Co})\text{O}_{3-\delta}$ perovskites. *Solid State Ion.* **2006**, *177*, 1753–1756. [[CrossRef](#)]
14. Yin, J.; Yin, Y.; Lu, J.; Zhang, C.; Minh, N.Q.; Ma, Z. Structure and Properties of Novel Cobalt-Free Oxides Temperature Solid Oxide Fuel Cells. *J. Phys. Chem. C* **2014**, *118*, 13357–13368. [[CrossRef](#)]
15. Jiang, S.P. Development of Lanthanum Strontium Manganite Perovskite Cathode Materials of Solid Oxide Fuel Cells: A Review. *J. Mater. Sci.* **2008**, *43*, 6799–6833. [[CrossRef](#)]
16. Li, X.; Jiang, X.; Xu, H.; Xu, Q.; Jiang, L.; Shi, Y.; Zhang, Q. Scandium-doped $\text{PrBaCo}_{2-x}\text{Sc}_x\text{O}_{6-\delta}$ oxides as cathode material for intermediate-temperature solid oxide fuel cells. *Int. J. Hydrog. Energy* **2013**, *38*, 12035–12042. [[CrossRef](#)]
17. Gumeci, C.; Parrondo, J.; Hussain, A.M.; Thompson, D.; Dale, N. Praseodymium based double-perovskite cathode nanofibers for intermediate temperature solid oxide fuel cells (IT-SOFC). *Int. J. Hydrog. Energy* **2021**, *46*, 31798–31806. [[CrossRef](#)]
18. Pelosato, R.; Cordaro, G.; Stucchi, D.; Cristiani, C.; Dotelli, G. Cobalt based layered perovskites as cathode material for intermediate temperature Solid Oxide Fuel Cells: A brief review. *J. Power Sources* **2015**, *298*, 46–67. [[CrossRef](#)]
19. Jin, F.; Li, L.; He, T. $\text{NdBaCo}_{2/3}\text{Fe}_{2/3}\text{Cu}_{2/3}\text{O}_{5+\delta}$ double perovskite as a novel cathode material for CeO_2 - and LaGaO_3 -based solid oxide fuel cells. *J. Power Sources* **2015**, *273*, 591–599. [[CrossRef](#)]
20. Bishop, S.R.; Marrocchelli, D.; Chatzichristodoulou, C.; Perry, N.H.; Mogensen, M.B.; Tuller, H.L.; Wachsman, E.D. Chemical expansion: Implications for electrochemical energy storage and conversion devices. *Annu. Rev. Mater. Res.* **2014**, *44*, 205–239. [[CrossRef](#)]
21. Bishop, S.R. Chemical expansion of solid oxide fuel cell materials: A brief overview. *Acta Mech.* **2013**, *29*, 312–317. [[CrossRef](#)]
22. Pan, Z.; Liu, Q.; Ni, M.; Lyu, R.; Li, P.; Chan, S.H. Activation and failure mechanism of $\text{La}_{0.6}\text{Sr}_{0.4}\text{Co}_{0.2}\text{Fe}_{0.8}\text{O}_{3-\delta}$ air electrode in solid oxide electrolyzer cells under high-current electrolysis. *Int. J. Hydrog. Energy* **2018**, *43*, 5437–5450. [[CrossRef](#)]
23. Monge, M.; Gil-Alana, L.A. Automobile components: Lithium and cobalt. Evidence of persistence. *Energy* **2019**, *169*, 489–495. [[CrossRef](#)]
24. Kim, J.H.; Manthiram, A. Layered $\text{LnBaCo}_2\text{O}_{5+\delta}$ perovskite cathodes for solid oxide fuel cells: An overview and perspective. *J. Mater. Chem.* **2015**, *3*, 24195–24210. [[CrossRef](#)]
25. Hashim, S.S.; Liang, F.; Zhou, W.; Sunarso, J. Cobalt-Free Perovskite Cathodes for Solid Oxide Fuel Cells. *Chem. Electro. Chem.* **2019**, *6*, 3549–3569. [[CrossRef](#)]
26. Baharuddin, N.A.; Muchtar, A.; Somalu, M.R. Short review on cobalt-free cathodes for solid oxide fuel cells. *Int. J. Hydrog. Energy* **2017**, *42*, 9149–9155. [[CrossRef](#)]
27. Niemczyk, A.; Du, Z.; Olszewska, A.; Marzec, M.; Gajewska, M.; Świerczek, K.; Zhao, H.; Poudel, B.; Dąbrowski, B. Effective oxygen reduction on A-site substituted $\text{LaCuO}_{3-\delta}$: Toward air electrodes for SOFCs based on perovskite-type copper oxides. *J. Mater. Chem. A* **2019**, *7*, 27403–27416. [[CrossRef](#)]

28. Li, K.; Niemczyk, A.; Świerczek, K.; Stepień, A.; Naumovich, Y.; Dąbrowa, J.; Zajusz, M.; Zheng, K.; Dabrowski, B. Co-free triple perovskite $\text{La}_{1.5}\text{Ba}_{1.5}\text{Cu}_3\text{O}_{7\pm\delta}$ as a promising air electrode material for solid oxide fuel cells. *J. Power Sources* **2022**, *532*, 231371. [CrossRef]
29. Kong, X.; Liu, G.; Yi, Z.; Ding, X. $\text{NdBaCu}_2\text{O}_{5+\delta}$ and $\text{NdBa}_{0.5}\text{Sr}_{0.5}\text{Cu}_2\text{O}_{5+\delta}$ layered perovskite oxides as cathode materials for IT-SOFCs. *Int. J. Hydrog. Energy* **2015**, *40*, 16477–16483. [CrossRef]
30. Kong, X.; Ding, X. Novel layered perovskite $\text{SmBaCu}_2\text{O}_{5+\delta}$ as a potential cathode for intermediate temperature solid oxide fuel cells. *Int. J. Hydrog. Energy* **2011**, *36*, 15715–15721. [CrossRef]
31. Ding, X.; Kong, X.; Wu, H.; Zhu, Y.; Tang, J.; Zhong, Y. $\text{SmBa}_{0.5}\text{Sr}_{0.5}\text{Cu}_2\text{O}_{5+\delta}$ and $\text{SmBa}_{0.5}\text{Sr}_{0.5}\text{CuFeO}_{5+\delta}$ layered perovskite oxides as cathodes for IT-SOFCs. *Int. J. Hydrog. Energy* **2012**, *37*, 2546–2551. [CrossRef]
32. Ding, P.; Li, W.; Zhao, H.; Wu, C.; Zhao, L.; Dong, B.; Wang, S. Review on Ruddlesden-Popper perovskites as cathode for solid oxide fuel cells. *J. Phys. Mater.* **2021**, *4*, 022002. [CrossRef]
33. Zheng, K.; Gorzkowska-Sobas, A.; Świerczek, K. Evaluation of Ln_2CuO_4 (Ln: La, Pr, Nd) oxides as cathode materials for IT-SOFCs. *Mater. Res. Bull.* **2012**, *47*, 4089–4095. [CrossRef]
34. Zheng, K.; Świerczek, K. Evaluation of $\text{La}_2\text{Ni}_{0.5}\text{Cu}_{0.5}\text{O}_{4+\delta}$ and $\text{Pr}_2\text{Ni}_{0.5}\text{Cu}_{0.5}\text{O}_{4+\delta}$ Ruddlesden-Popper-type layered oxides as cathode materials for solid oxide fuel cells. *Mater. Res. Bull.* **2016**, *84*, 259–266. [CrossRef]
35. Gędziorowski, B.; Cichy, K.; Niemczyk, A.; Olszewska, A.; Zhang, Z.; Kopeć, S.; Zheng, K.; Marzec, M.; Gajewska, M.; Du, Z.; et al. Ruddlesden-Popper-type $\text{Nd}_{2-x}\text{Ni}_{1-y}\text{Cu}_y\text{O}_{4\pm\delta}$ layered oxides as candidate materials for MIEC-type ceramic membranes. *J. Eur. Ceram. Soc.* **2020**, *40*, 4056–4066. [CrossRef]
36. Zhou, J.S.; Marshall, L.G.; Goodenough, J.B. Mass enhancement versus Stoner enhancement in strongly correlated metallic perovskites: LaNiO_3 and LaCuO_3 . *Phys. Rev. B* **2014**, *89*, 245138. [CrossRef]
37. Weigl, C.; Range, K.-J. Rhombohedral LaCuO_3 : High-pressure synthesis of single crystals and structure refinement. *J. Alloy. Compd.* **1993**, *200*, L1–L2. [CrossRef]
38. Karppinen, M.; Yamauchi, H.; Ito, T.; Suematsu, H.; Fukunaga, O. High-pressure synthesis and thermal decomposition of LaCuO_3 . *Mater. Sci. Eng. B* **1996**, *41*, 59–62. [CrossRef]
39. Liu, Y.X.; Wang, S.F.; Hsu, Y.F.; Kai, H.W.; Jasinski, P. Characteristics of $\text{LaCo}_{0.4}\text{Ni}_{0.6-x}\text{Cu}_x\text{O}_{3-\delta}$ ceramics as a cathode material for intermediate-temperature solid oxide fuel cells. *J. Eur. Ceram. Soc.* **2018**, *38*, 1654–1662. [CrossRef]
40. Niemczyk, A.; Zheng, K.; Cichy, K.; Berent, K.; Kuster, K.; Starke, U.; Poudel, B.; Dabrowski, B.; Świerczek, K. High Cu content $\text{LaNi}_{1-x}\text{Cu}_x\text{O}_{3-\delta}$ perovskites as candidate air electrode materials for Reversible Solid Oxide Cells. *Int. J. Hydrog. Energy* **2020**, *45*, 29449–29464. [CrossRef]
41. Ren, Y.; Küngas, R.; Gorte, R.J.; Deng, C. The effect of A-site cation (Ln = La, Pr, Sm) on the crystal structure, conductivity and oxygen reduction properties of Sr-doped ferrite perovskites. *Solid State Ion.* **2012**, *212*, 47–54. [CrossRef]
42. Wang, S.; Li, Z.; Qian, B.; Ni, Q.; Zheng, Y.; Ge, L.; Chen, H.; Yang, H. Evaluation of Cu-substituted $\text{La}_{1.5}\text{Sr}_{0.5}\text{NiO}_{4+\delta}$ as air electrode for CO_2 electrolysis in solid oxide electrolysis cells. *Ceram. Int.* **2022**, *48*, 31509–31518. [CrossRef]
43. Shen, Y.; Zhao, H.; Xu, J.; Zhang, X.; Zheng, K.; Świerczek, K. Effect of ionic size of dopants on the lattice structure, electrical and electrochemical properties of $\text{La}_{2-x}\text{M}_x\text{NiO}_{4+\delta}$ (M = Ba, Sr) cathode materials. *Int. J. Hydrog. Energy* **2014**, *39*, 1023–1029. [CrossRef]
44. Muñoz-García, A.B.; Ritzmann, A.M.; Pavone, M.; Keith, J.A.; Carter, E.A. Oxygen transport in perovskite-type solid oxide fuel cell materials: Insights from quantum mechanics. *Acc. Chem. Res.* **2014**, *47*, 3340–3348. [CrossRef] [PubMed]
45. Larson, A.C.; Von Dreele, R.B. General Structure Analysis System (GSAS). Los Alamos National Laboratory LAUR 86-748, 2004. Available online: <https://11bm.xray.aps.anl.gov/documents/GSASManual.pdf> (accessed on 1 November 2022).
46. Toby, B.H. EXPGUL, a graphical user interface for GSAS. *J. Appl. Crystallogr.* **2001**, *34*, 210–213. Available online: <https://doi.org/10.1107/S0021889801002242> (accessed on 1 November 2022). [CrossRef]
47. Xiao, J.; Zeng, X.; Li, M.; Dong, P.; Wo, H.; Xu, M.; Lin, Y.; Liu, J.; Xie, Y.; Zhang, Y. Effect of pre-calcined ceramic powders at different temperatures on Ni-YSZ anode-supported SOFC cell/stack by low pressure injection molding. *Ceram. Int.* **2019**, *45*, 20066–20072. [CrossRef]
48. Kupecki, J.; Kluczowski, R.; Papurello, D.; Lanzini, A.; Kawalec, M.; Krauz, M.; Santarelli, M. Characterization of a circular 80 mm anode supported solid oxide fuel cell (AS-SOFC) with anode support produced using high-pressure injection molding (HPIM). *Int. J. Hydrog. Energy* **2019**, *44*, 19405–19411. [CrossRef]
49. Motylinski, K.; Wierzbicki, M.; Kupecki, J.; Jagielski, S. Investigation of off-design characteristics of solid oxide electrolyser (SOE) operating in endothermic conditions. *Renew. Energy* **2021**, *170*, 277–285. [CrossRef]
50. Nielsen, J.; Hjelm, J. Impedance of SOFC electrodes: A review and a comprehensive case study on the impedance of LSM:YSZ cathodes. *Electrochim. Acta* **2014**, *115*, 31–45. [CrossRef]
51. Retuerto, M.; Pereira, A.G.; Peérez-Alonso, F.J.; Peña, M.A.; Fierro, J.L.G.; Alonso, J.A.; Fernández-Díaz, M.T.; Pascual, L.; Rojas, S. Structural effects of LaNiO_3 as electrocatalyst for the oxygen reduction reaction. *Appl. Catal. B Environ.* **2017**, *203*, 363–371. [CrossRef]
52. Marrocchelli, D.; Perry, N.H.; Bishop, S.R. Understanding chemical expansion in perovskite-structured oxides. *Phys. Chem. Chem. Phys.* **2015**, *17*, 10028–10039. [CrossRef]
53. Karim, D.P.; Aldred, A.T. Localized level hopping transport in $\text{La}(\text{Sr})\text{CrO}_3$. *Phys. Rev. B* **1979**, *20*, 2255–2263. [CrossRef]
54. Jemai, R.; Wederni, M.A.; Amorri, O.; Hzez, W.; Martín-Palma, R.J.; Khirouni, K. Effects of doping by copper on electrical properties of LaCrO_3 based perovskite. *Ceram. Int.* **2022**, *48*, 14050–14059. [CrossRef]

55. Vibhu, V.; Flura, A.; Nicollet, C.; Fourcade, S.; Penin, N.; Bassat, J.M.; Grenier, J.-C.; Rougier, A.; Pouchard, M. Characterization of PrNiO_{3-d} as oxygen electrode for SOFCs. *Solid State Sci.* **2018**, *81*, 26–31. [[CrossRef](#)]
56. Boehm, E.; Bassat, J.M.; Steil, M.C.; Dordor, P.; Mauvy, F.; Grenier, J.C. Oxygen transport properties of $\text{La}_2\text{Ni}_{1-x}\text{Cu}_x\text{O}_{4-d}$ mixed conducting oxides. *Solid State Sci.* **2003**, *5*, 973–981. [[CrossRef](#)]
57. Zheng, K.; Świerczek, K. Physicochemical properties of rock salt-type ordered Sr_2MMoO_6 (M = Mg, Mn, Fe, Co, Ni) double perovskites. *J. Eur. Ceram. Soc.* **2014**, *34*, 4273–4284. [[CrossRef](#)]
58. Sun, C.; Hui, R.; Roller, J. Cathode materials for solid oxide fuel cells: A review. *J. Solid. State. Electrochem.* **2010**, *14*, 1125–1144. [[CrossRef](#)]
59. Kuroda, C.; Zheng, K.; Świerczek, K. Characterization of novel $\text{GdBa}_{0.5}\text{Sr}_{0.5}\text{Co}_{2-x}\text{Fe}_x\text{O}_{5+\delta}$ perovskites for application in IT-SOFC cells. *Int. J. Hydrog. Energy* **2013**, *38*, 1027–1038. [[CrossRef](#)]
60. Yaremchenko, A.; Arias-Serrano, B.I.; Zakharchuk, K.; Frade, J.R. Perovskite-like $\text{LaNiO}_{3-\delta}$ as Oxygen Electrode Material for Solid Oxide Electrolysis Cells. *ECS Trans.* **2019**, *91*, 2399. [[CrossRef](#)]
61. Rehman, S.U.; Shaur, A.; Song, R.-H.; Lim, T.-H.; Hong, J.-E.; Park, S.-J.; Lee, S.-B. Nano-fabrication of a high-performance LaNiO_3 cathode for solid oxide fuel cells using an electrochemical route. *J. Power Sources* **2019**, *429*, 97–104. [[CrossRef](#)]
62. Hussain, M.; Muneer, M.; Abbas, G.; Shakir, I.; Iqbal, A.; Javed, M.A.; Iqbal, M.; Rehman, Z.U.; Raza, R. Cobalt free $\text{La}_x\text{Sr}_{1-x}\text{Fe}_{1-y}\text{Cu}_y\text{O}_{3-\delta}$ ($x = 0.54, 0.8, y = 0.2, 0.4$) perovskite structured cathode for SOFC. *Ceram. Int.* **2020**, *46*, 18208–18215. [[CrossRef](#)]
63. Zhu, Z.; Qian, J.; Wang, Z.; Dang, J.; Liu, W. High-performance anode-supported solid oxide fuel cells based on nickel-based cathode and $\text{Ba}(\text{Zr}_{0.1}\text{Ce}_{0.7}\text{Y}_{0.2})\text{O}_{3-\delta}$ electrolyte. *J. Alloy. Compd.* **2013**, *581*, 832–835. [[CrossRef](#)]
64. Vidal, K.; Morán-Ruiz, A.; Larrañaga, A.; Porras-Vázquez, J.M.; Slater, P.R.; Arriortua, M.I. Characterization of $\text{LaNi}_{0.6}\text{Fe}_{0.4}\text{O}_3$ perovskite synthesized by glycine-nitrate combustion method. *Solid State Ion.* **2015**, *269*, 24–29. [[CrossRef](#)]
65. Bo, L.; Na, L.; Liping, S.; Qiang, L.; Lihua, H.; Hui, Z. Rare-earth elements doped Nd_2CuO_4 as Cu-based cathode for intermediate-temperature solid oxide fuel cells. *J. Alloy. Compd.* **2021**, *870*, 159397. [[CrossRef](#)]
66. Meng, X.; Lü, S.; Yu, W.W.; Ji, Y.; Sui, Y.; Wei, M. Layered perovskite $\text{LnBa}_{0.5}\text{Sr}_{0.5}\text{Cu}_2\text{O}_{5+\delta}$ (Ln = Pr and Nd) as cobalt-free cathode materials for solid oxide fuel cells. *Int. J. Hydrog. Energy* **2018**, *43*, 4458–4470. [[CrossRef](#)]
67. Han, J.; Zheng, K.; Świerczek, K. Nickel-based layered perovskite cathode materials for application in intermediate-temperature solid oxide fuel cells. *Funct. Mater. Lett.* **2011**, *4*, 151–155. [[CrossRef](#)]
68. Pikalova, E.; Kolchugin, A.; Bogdanovich, N.; Medvedev, D.; Lyagaeva, J.; Vedmid, L.; Ananyev, M.; Plaksin, S.; Farlenkov, A. Suitability of $\text{Pr}_{2-x}\text{Ca}_x\text{NiO}_{4+\delta}$ as cathode materials for electrochemical devices based on oxygen ion and proton conducting solid state electrolytes. *Int. J. Hydrog. Energy* **2020**, *45*, 13612–13624. [[CrossRef](#)]
69. Liu, M.; Dong, D.; Zhao, F.; Gao, J.; Ding, D.; Liu, X.; Meng, G. High-performance cathode-supported SOFCs prepared by a single-step co-firing process. *J. Power Sources* **2008**, *182*, 585–588. [[CrossRef](#)]
70. Zhang, X.; Lin, B.; Ling, Y.; Dong, Y.; Meng, G.; Liu, X. An anode-supported hollow fiber solid oxide fuel cell with $(\text{Pr}_{0.5}\text{Nd}_{0.5})_{0.7}\text{Sr}_{0.3}\text{MnO}_{3-\delta}$ -YSZ composite cathode. *J. Alloy. Compd.* **2010**, *497*, 386–389. [[CrossRef](#)]
71. Zheng, K.; Lach, J.; Zhao, H.; Huang, X.; Qi, K. Magnesium-Doped $\text{Sr}_2(\text{Fe},\text{Mo})\text{O}_{6-\delta}$ Double Perovskites with Excellent Redox Stability as Stable Electrode Materials for Symmetrical Solid Oxide Fuel Cells. *Membranes* **2022**, *12*, 1006. [[CrossRef](#)]
72. Liu, H.; Zhu, K.; Liu, Y.; Li, W.; Cai, L.; Zhu, X.; Cheng, M.; Yang, W. Structure and electrochemical properties of cobalt-free perovskite cathode materials for intermediate-temperature solid oxide fuel cells. *Electrochim. Acta* **2018**, *279*, 224–230. [[CrossRef](#)]